Communications in Applied Mathematics and Computational Science

AN ADAPTIVE MULTIBLOCK HIGH-ORDER FINITE-VOLUME METHOD FOR SOLVING THE SHALLOW-WATER EQUATIONS ON THE SPHERE

PETER MCCORQUODALE, PAUL A. ULLRICH, HANS JOHANSEN AND PHILLIP COLELLA

vol. 10 no. 2 2015

msp

COMM. APP. MATH. AND COMP. SCI.
Vol. 10, No. 2, 2015
dx.doi.org/10.2140/camcos.2015.10.121

AN ADAPTIVE MULTIBLOCK HIGH-ORDER FINITE-VOLUME METHOD FOR SOLVING THE SHALLOW-WATER EQUATIONS ON THE SPHERE

PETER MCCORQUODALE, PAUL A. ULLRICH,
HANS JOHANSEN AND PHILLIP COLELLA

We present a high-order finite-volume approach for solving the shallow-water equations on the sphere, using multiblock grids on the cubed sphere. This approach combines a Runge–Kutta time discretization with a fourth-order-accurate spatial discretization and includes adaptive mesh refinement and refinement in time. Results of tests show fourth-order convergence for the shallow-water equations as well as for advection in a highly deformational flow. Hierarchical adaptive mesh refinement allows solution error to be achieved that is comparable to that obtained with uniform resolution of the most refined level of the hierarchy but with many fewer operations.

1. Introduction

In this paper, we present a method of local refinement applied to the 2D shallow-water equations, using test cases that capture some of the essential features that arise in 3D atmospheric models. We extend a uniform-grid finite-volume discretization on the surface of a sphere to a locally refined, nested grid hierarchy that can evolve in time, and can therefore resolve or track small-scale and synoptic features, without refining the entire computational domain. Similar high-accuracy block-structured adaptive mesh refinement (AMR) approaches have been applied to problems in compressible gas dynamics [32; 19]. For climate applications, AMR techniques hold the promise of spanning global and regional scales as well as tracking synoptic features that contribute significantly to climate means in the Earth system. Computational cost limits the finest resolution of uniform-resolution climate models to around 10 km, far larger than the grid spacing necessary for resolving clouds and features of regional climate. The highest-resolution simulations have become

This work was supported by the Director, Office of Science, Office of Advanced Scientific Computing Research, of the United States Department of Energy under Contract Number DE-AC02-05CH11231.
MSC2010: primary 35L40, 65M50, 65M08; secondary 35L65, 86-08.
Keywords: high order, finite-volume method, cubed sphere, shallow-water equations, adaptive mesh refinement.

important for regional planning issues, which rely on accurate representation of changes in the behavior of mesoscale storm systems, pressure-blocking events driven by topography (responsible for heat waves and cold spells), mountain snowpack, wildfires, topographically driven precipitation, watershed-level hydrology, and urban development and agriculture. As emphasized in [58], addressing these challenges requires high-resolution regional climate modeling via either dynamical downscaling or highly refined grids. Moving synoptic features, such as extratropical and tropical cyclones, would benefit from space-time adaptivity to better resolve their dynamics. Thus, AMR can both improve the resolution of atmospheric flows and help test physical parametrizations across spatial and temporal scales in a global context, without refining the entire computational domain.

As a first step in the development of a global atmospheric modeling system, in this paper, we solve the 2D shallow-water equations, which capture many of the important properties of the equations of motion for the atmosphere. In particular, the dynamical character of the global shallow-water equations is governed by features common with atmospheric motions, including barotropic Rossby waves and inertia-gravity waves, without the added complexity of a vertical dimension. There already exists a comprehensive literature on the development of numerical methods for the global shallow-water equations spanning the past several decades. Examples include the spectral-transform method [25], semi-Lagrangian methods [41; 4; 53; 63; 54; 38], finite-difference methods [21; 42], Godunov-type finite-volume methods [43; 57], staggered finite-volume methods [29; 39; 40], multimoment finite-volume methods [8; 27; 7], and finite-element methods [51; 12; 52; 17; 33; 26; 11; 2].

As of the time of writing, work targeting AMR for the global shallow-water equations is much more sparse. Two adaptive numerical methods (finite-volume on a latitude-longitude grid and nonconservative finite-element on a cubed-sphere grid) are described in [49]. A discontinuous Galerkin formulation for global tsunami simulation is described in [5]. The multimoment finite-volume approach has also been extended to an adaptive formulation by [9]. The present article introduces an AMR approach for the shallow-water equations that also supports refinement in time.

Atmospheric models include a wide variety of computational grids on the sphere such as the latitude-longitude mesh [62; 28], icosahedral and hexagonal grids [16; 48; 18; 45; 59], and cubed-sphere meshes [56; 13; 36]. In particular, icosahedral, hexagonal, and cubed-sphere meshes have become popular over the last decade as they provide an almost-regular grid-point coverage on the sphere. The uniform distribution of elements avoids the coordinate singularities at the poles that complicate the design of stable and accurate methods for such coordinate systems.

The approach in this paper is based on the finite-volume mapped-grid technology in [10], which is extended to work with AMR in [19]. We apply these methods on cubed-sphere meshes, which consist of six panels with a separate mapping on each

panel. To coordinate the different mappings along panel boundaries, we use the mapped-multiblock approach of [31] with the following modifications:

(1) Because the computational domain is on the surface of a sphere, which is a 2D manifold in a 3D space, the evolution equations must include metric terms.

(2) Because we have vector quantities (velocities and momenta) that are expressed in different bases on different panels, the procedure for coordinating them across a panel boundary must include a basis transformation.

For smooth solutions, this approach can provide fourth-order-accurate results as also achieved in [57]. Comparing these results to those of [43] shows the advantage of fourth-order over second-order methods in avoiding artifacts at the boundaries of the cubed-sphere panels. The dispersive properties of this method have been analyzed by [55], where it was demonstrated that the use of a fourth-order finite-volume discretization led to a doubling of the effective resolution compared to a second-order approach. High-order accuracy is also necessary in the context of grid refinement since there is a formal drop of one order of accuracy (in the maximum norm) at grid-refinement boundaries. Hence, a second-order adaptive method would drop to first-order accuracy in the presence of grid refinement, with disastrous consequences to the quality of the solution, whereas a fourth-order method only drops to third-order. Further, compared to other numerical methods, including standard finite-element discretizations, central finite-volume methods provide the largest maximum stable time-step size and do not suffer from issues such as the "spectral gap" that arise from nonuniform treatments. In the absence of limiters and explicit dissipation, these schemes are also energy-conservative up to temporal truncation order.

2. Partial differential equations in cubed-sphere coordinates

The equiangular cubed-sphere grid [44; 42] consists of a cube with six Cartesian patches arranged along each face, which is then "deflated" onto a tangent spherical shell, as shown in Figure 1. It is a *quasiuniform spherical grid*; that is, it is in the class of grids that provide an approximately uniform tiling of the sphere (see [50], for example, for a review of different options for global grids). The equiangular cubed-sphere grid has the advantage of being among the most uniform of cubed-sphere grids: at high resolutions, the ratio of largest to smallest grid cell approaches $\sqrt{2}$, compared to the equidistant gnomonic cubed-sphere grid, which approaches a ratio of $3\sqrt{3}$, and the conformal cubed-sphere grid, where this ratio is unbounded. Although even more uniformity can be attained via the application of grid-relaxation techniques such as spring dynamics (see, for example, [37]), these techniques also lead to nonanalytical forms of the curvature metrics, which in turn increases the complexity of the discretization.

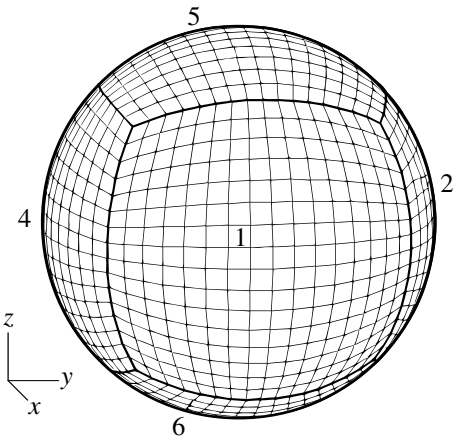

Figure 1. A cubed-sphere grid, shown with labels on panels. Panels 1–4 all straddle the equator ($z = 0$) of the unit sphere. Panel 5 is centered on the north pole ($z = +1$) and Panel 6 on the south pole ($z = -1$). On the cubed-sphere grid shown here, $N_c = 16$ (each panel contains 16×16 grid cells).

On the equiangular cubed-sphere grid, coordinates are given as (α, β, n_p), with central angles $\alpha, \beta \in [-\pi/4, \pi/4]$ and panel index $n_p \in \{1, 2, 3, 4, 5, 6\}$. By convention, we choose Panels 1–4 to be along the equator and Panels 5 and 6 to be centered on the northern and southern poles, respectively.

We will also use spherical coordinates (λ, ϕ) with longitude $\lambda \in [0, 2\pi]$ and latitude $\phi \in [-\pi/2, \pi/2]$ for plotting and specification of tests. Coordinate transforms between spherical and equiangular coordinates can be found in [56, Appendix A].

2.1. ***Metrics.*** Coordinates (X, Y) are related to equiangular coordinates (α, β) via the transform

$$X = \tan\alpha, \qquad Y = \tan\beta. \tag{1}$$

Any straight line in (X, Y) coordinates is also a great circle arc, which is not the case for general line segments in equiangular coordinates. Throughout this paper, we will be making use of the metric term

$$\delta = (1 + \tan^2\alpha + \tan^2\beta)^{1/2}, \tag{2}$$

which appears frequently in geometric calculations on the cubed-sphere grid.

Cartesian coordinates are related to the equiangular coordinates of a particular cubed-sphere panel by $\boldsymbol{x}(\alpha, \beta) = (x(\alpha, \beta), y(\alpha, \beta), z(\alpha, \beta))$. The natural basis vectors of the equiangular coordinate system are $\boldsymbol{g}_\alpha = (\partial \boldsymbol{x}/\partial\alpha)_\beta$ and $\boldsymbol{g}_\beta = (\partial \boldsymbol{x}/\partial\beta)_\alpha$, which have units of length.

The covariant 2D metric on the cubed sphere of radius r is given by

$$g_{pq} = \boldsymbol{g}_p \cdot \boldsymbol{g}_q = \frac{r^2(1+X^2)(1+Y^2)}{\delta^4} \begin{pmatrix} 1+X^2 & -XY \\ -XY & 1+Y^2 \end{pmatrix}, \tag{3}$$

with contravariant inverse

$$g^{pq} = \frac{\delta^2}{r^2(1+X^2)(1+Y^2)} \begin{pmatrix} 1+Y^2 & XY \\ XY & 1+X^2 \end{pmatrix}. \tag{4}$$

The Jacobian on the manifold is then

$$J = \sqrt{\det g_{pq}} = \frac{r^2(1+X^2)(1+Y^2)}{\delta^3} \tag{5}$$

and induces the infinitesimal area element $dA = J\, d\alpha\, d\beta$.

For a comprehensive mathematical description of the equiangular cubed-sphere grid, see [33, Appendices A, B, and C] or [56, Appendices A and B].

2.2. ***The shallow-water equations in cubed-sphere coordinates.*** In conservative coordinate-invariant form, the 2D shallow-water equations on the sphere can be written as

$$\frac{\partial H}{\partial t} + \nabla \cdot (h\boldsymbol{u}) = 0, \tag{6}$$

$$\frac{\partial h\boldsymbol{u}}{\partial t} + \nabla \cdot \left(h\boldsymbol{u}\boldsymbol{u} + \mathcal{I}\frac{Gh^2}{2} \right) = -Gh\nabla z_s - f\boldsymbol{g}_r \times (h\boldsymbol{u}), \tag{7}$$

where H denotes the fluid surface height above the reference depth $z = 0$, h is the fluid depth above the bottom topography $z = z_s(\lambda, \phi)$, $\boldsymbol{u}$ is the velocity vector, $\boldsymbol{u}\boldsymbol{u}$ denotes the outer product of the velocity, $\mathcal{I}$ is the identity matrix, $G = 9.80616\,\mathrm{m\cdot s^{-2}}$ is the acceleration due to gravity, $f = 2\Omega \sin\phi$ is the Coriolis parameter in terms of the rotation rate $\Omega = 7.292 \times 10^{-5}\,\mathrm{s^{-1}}$, and $\boldsymbol{g}_r$ is the unit vector perpendicular to the surface of the sphere. The quantities H, h, and z_s are related via $H = h + z_s$.

Under equiangular coordinates, the velocity field is written as

$$\boldsymbol{u} = u^\alpha \boldsymbol{g}_\alpha + u^\beta \boldsymbol{g}_\beta. \tag{8}$$

The coefficients u^α and u^β are known as the contravariant components of the velocity vector and have units of rad/s in the natural basis.

The height evolution equation (6) then takes the form

$$\frac{\partial H}{\partial t} + \frac{1}{J}\frac{\partial}{\partial \alpha}(Jhu^\alpha) + \frac{1}{J}\frac{\partial}{\partial \beta}(Jhu^\beta) = 0. \tag{9}$$

The momentum evolution equation (7) can be decomposed into an evolution equation for hu^α and hu^β,

$$\frac{\partial}{\partial t}\begin{pmatrix} hu^\alpha \\ hu^\beta \end{pmatrix} + \frac{1}{J}\frac{\partial}{\partial \alpha}\begin{pmatrix} J\mathcal{T}^{\alpha\alpha} \\ J\mathcal{T}^{\beta\alpha} \end{pmatrix} + \frac{1}{J}\frac{\partial}{\partial \beta}\begin{pmatrix} J\mathcal{T}^{\alpha\beta} \\ J\mathcal{T}^{\beta\beta} \end{pmatrix} = \boldsymbol{\Psi}_M + \boldsymbol{\Psi}_B + \boldsymbol{\Psi}_C, \tag{10}$$

where $\mathcal{T}^{kn} = hu^k u^n + g^{kn}\frac{1}{2}Gh^2$ and $\boldsymbol{\Psi}_M$, $\boldsymbol{\Psi}_B$, and $\boldsymbol{\Psi}_C$ denote source terms due to the curvature of the manifold, bottom topography, and Coriolis force, respectively.

The manifold source term takes the form

$$\boldsymbol{\Psi}_{\mathrm{M}} = \begin{pmatrix} -\Gamma^{\alpha}_{\ nk}\mathcal{T}^{kn} \\ -\Gamma^{\beta}_{\ nk}\mathcal{T}^{kn} \end{pmatrix} = \frac{2}{\delta^2}\begin{pmatrix} -XY^2 hu^{\alpha}u^{\alpha} + Y(1+Y^2)hu^{\alpha}u^{\beta} \\ X(1+X^2)hu^{\alpha}u^{\beta} - X^2 Y hu^{\beta}u^{\beta} \end{pmatrix}, \tag{11}$$

where $\Gamma^{m}_{\ nk}$ are the Christoffel symbols of the second kind associated with the metric. The source term due to bottom topography can be written in terms of derivatives of z_{s} as

$$\boldsymbol{\Psi}_{\mathrm{B}} = -Gh\begin{pmatrix} g^{\alpha k}\nabla_k z_{\mathrm{s}} \\ g^{\beta k}\nabla_k z_{\mathrm{s}} \end{pmatrix} = -Gh\begin{pmatrix} g^{\alpha\alpha} & g^{\alpha\beta} \\ g^{\beta\alpha} & g^{\beta\beta} \end{pmatrix}\begin{pmatrix} \partial z_{\mathrm{s}}/\partial\alpha \\ \partial z_{\mathrm{s}}/\partial\beta \end{pmatrix}. \tag{12}$$

The Coriolis source term differs depending on whether the underlying panel is equatorial or polar since

$$\sin\phi = \begin{cases} Y/\delta & \text{if } n_{\mathrm{p}} \in \{1,2,3,4\}, \\ p/\delta & \text{if } n_{\mathrm{p}} \in \{5,6\}, \end{cases} \tag{13}$$

where p is a panel indicator given by, for instance,

$$p = \operatorname{sign}\phi = \begin{cases} +1 & \text{on the northern panel } (n_{\mathrm{p}} = 5), \\ -1 & \text{on the southern panel } (n_{\mathrm{p}} = 6). \end{cases} \tag{14}$$

For equatorial panels, the Coriolis source term is given by

$$\boldsymbol{\Psi}_{\mathrm{C,eq}} = \frac{2\Omega}{\delta^2}\begin{pmatrix} -XY^2 & Y(1+Y^2) \\ -Y(1+X^2) & XY^2 \end{pmatrix}\begin{pmatrix} hu^{\alpha} \\ hu^{\beta} \end{pmatrix} \tag{15}$$

and on polar panels by

$$\boldsymbol{\Psi}_{\mathrm{C,pol}} = \frac{2p\Omega}{\delta^2}\begin{pmatrix} -XY & (1+Y^2) \\ -(1+X^2) & XY \end{pmatrix}\begin{pmatrix} hu^{\alpha} \\ hu^{\beta} \end{pmatrix}. \tag{16}$$

Multiplying both sides of the shallow-water equations (9)–(10) by J and using the fact that J and the topography $z_{\mathrm{s}} = H - h$ are independent of t, these evolution equations can be written

$$\frac{\partial}{\partial t}(J\boldsymbol{U}) + \nabla\cdot(J\vec{\boldsymbol{F}}) = J\boldsymbol{\Psi}, \tag{17}$$

where

$$\boldsymbol{U} = \begin{pmatrix} h \\ hu^{\alpha} \\ hu^{\beta} \end{pmatrix}, \qquad \boldsymbol{F}^k = \begin{pmatrix} hu^k \\ \mathcal{T}^{\alpha k} \\ \mathcal{T}^{\beta k} \end{pmatrix}, \qquad \boldsymbol{\Psi} = \begin{pmatrix} 0 \\ \boldsymbol{\Psi}_{\mathrm{M}} + \boldsymbol{\Psi}_{\mathrm{B}} + \boldsymbol{\Psi}_{\mathrm{C}} \end{pmatrix}. \tag{18}$$

Here $\boldsymbol{U}$ contains the *conserved* variables, which are functions of the *primitive* variables,

$$\boldsymbol{W} = \begin{pmatrix} h \\ u^\alpha \\ u^\beta \end{pmatrix}. \tag{19}$$

The components of $\vec{\boldsymbol{F}}$ are functions of the primitive variables and the metric.

2.3. ***Advection in cubed-sphere coordinates.*** In conservative coordinate-invariant form, the 2D advection equation on the sphere is just the first equation of (17):

$$\frac{\partial}{\partial t}(J\boldsymbol{U}) + \nabla \cdot (J\vec{\boldsymbol{F}}) = 0 \tag{20}$$

with only one component, $\boldsymbol{U} = h$ and $\boldsymbol{F}^k = hu^k$. Here, h is interpreted as the density of the advected quantity, and $\boldsymbol{u}(\alpha, \beta, t)$ is a prescribed velocity vector field.

3. Finite-volume discretization on cubed-sphere grids

3.1. ***Discretization of the cubed sphere.*** The discrete resolution of the cubed sphere is typically written in the form c$\{N_c\}$, where each coordinate direction consists of N_c grid cells. For instance, the cubed-sphere grid shown in Figure 1 is c16. The total number of grid cells on a cubed sphere is $N_c \times N_c \times 6$. A grid cell on a particular panel is denoted by $V_{i,j}$ with indices $(i, j) \in [0, \ldots, N_c - 1]^2$, which refers to the region bounded by

$$\alpha \in [i\Delta\alpha - \tfrac{1}{4}\pi, (i+1)\Delta\alpha - \tfrac{1}{4}\pi], \qquad \beta \in [j\Delta\beta - \tfrac{1}{4}\pi, (j+1)\Delta\beta - \tfrac{1}{4}\pi], \tag{21}$$

where on an equiangular grid the grid spacing is

$$\Delta\alpha = \Delta\beta = \frac{\pi}{2N_c}. \tag{22}$$

The center of $V_{i,j}$ is the point (α_i, β_j) with

$$\alpha_i = (i + \tfrac{1}{2})\Delta\alpha - \tfrac{1}{4}\pi, \qquad \beta_j = (j + \tfrac{1}{2})\Delta\beta - \tfrac{1}{4}\pi. \tag{23}$$

Some properties of the cubed-sphere grid for a variety of resolutions are given in Table 1.

3.2. ***PDE discretization.*** We can integrate a PDE of the form

$$\frac{\partial}{\partial t}(J\boldsymbol{U}) + \nabla \cdot (J\vec{\boldsymbol{F}}) = J\boldsymbol{\Psi} \tag{24}$$

over a grid cell $V_{i,j}$, giving

$$\frac{d}{dt}\iint_{V_{i,j}} J\boldsymbol{U}\, d\alpha\, d\beta + \iint_{V_{i,j}} \nabla \cdot (J\vec{\boldsymbol{F}})\, d\alpha\, d\beta = \iint_{V_{i,j}} J\boldsymbol{\Psi}\, d\alpha\, d\beta. \tag{25}$$

Resolution	Δx	A_{avg}	$A_{\text{min}}/A_{\text{max}}$	$\text{RLL}_{\text{equiv}}$	T_{equiv}
c16	625 km	3.321×10^5 km^2	0.7434	6.5°	$T17$
c32	313 km	8.302×10^4 km^2	0.7249	3.2°	$T34$
c64	156 km	2.076×10^4 km^2	0.7159	1.6°	$T68$
c128	78.2 km	5.189×10^3 km^2	0.7115	0.82°	$T136$
c256	39.1 km	1.297×10^3 km^2	0.7093	0.41°	$T272$

Table 1. Properties of the cubed-sphere grid for different resolutions. Here Δx is the grid spacing at the equator, A_{avg} is the average area of all cubed-sphere grid cells, A_{min} is the minimum cell area, and A_{max} is the maximum cell area. $\text{RLL}_{\text{equiv}}$ denotes the equivalent grid spacing (in degrees) on the regular latitude-longitude grid with the same number of cells, and T_{equiv} denotes the approximate triangular truncation of a spectral transform method.

Then applying the divergence theorem to the second term on the left-hand side of (25):

$$\frac{d}{dt}\iint_{V_{i,j}} J\boldsymbol{U}\,d\alpha\,d\beta + \oint_{\partial V_{i,j}} J\vec{\boldsymbol{F}}\cdot\hat{\boldsymbol{n}}\,d\ell = \iint_{V_{i,j}} J\boldsymbol{\Psi}\,d\alpha\,d\beta. \tag{26}$$

We can represent the integrals in (26) in terms of averages over $V_{i,j}$ and its faces. The notation for an average of a quantity $A(\alpha,\beta)$ over $V_{i,j}$ is

$$\langle A\rangle_{i,j} = \frac{\displaystyle\iint_{V_{i,j}} A(\alpha,\beta)\,d\alpha\,d\beta}{\displaystyle\iint_{V_{i,j}} d\alpha\,d\beta} = \frac{\displaystyle\int_{\beta_j-\frac{1}{2}\Delta\beta}^{\beta_j+\frac{1}{2}\Delta\beta}\int_{\alpha_i-\frac{1}{2}\Delta\alpha}^{\alpha_i+\frac{1}{2}\Delta\alpha} A(\alpha,\beta)\,d\alpha\,d\beta}{\Delta\alpha\,\Delta\beta}. \tag{27}$$

Averages over faces of $V_{i,j}$ with constant $\alpha = \alpha_i \pm \frac{1}{2}\Delta\alpha$ and $\beta = \beta_j \pm \frac{1}{2}\Delta\beta$ are denoted, respectively,

$$\langle A\rangle_{i\pm\frac{1}{2},j} = \frac{\displaystyle\int_{\beta_j-\frac{1}{2}\Delta\beta}^{\beta_j+\frac{1}{2}\Delta\beta} A(\alpha_i \pm \tfrac{1}{2}\Delta\alpha,\beta)\,d\beta}{\Delta\beta}, \tag{28}$$

$$\langle A\rangle_{i,j\pm\frac{1}{2}} = \frac{\displaystyle\int_{\alpha_i-\frac{1}{2}\Delta\alpha}^{\alpha_i+\frac{1}{2}\Delta\alpha} A(\alpha,\beta_j \pm \tfrac{1}{2}\Delta\beta)\,d\alpha}{\Delta\alpha}. \tag{29}$$

Then dividing both sides of (26) by $\Delta\alpha\,\Delta\beta$ and substituting the averages as defined in (27)–(29):

$$\frac{d}{dt}\langle J\boldsymbol{U}\rangle_{i,j} = -\frac{1}{\Delta\alpha}\left(\langle J\boldsymbol{F}^{\alpha}\rangle_{i+\frac{1}{2},j} - \langle J\boldsymbol{F}^{\alpha}\rangle_{i-\frac{1}{2},j}\right) - \frac{1}{\Delta\beta}\left(\langle J\boldsymbol{F}^{\beta}\rangle_{i,j+\frac{1}{2}} - \langle J\boldsymbol{F}^{\beta}\rangle_{i,j-\frac{1}{2}}\right) + \langle J\boldsymbol{\Psi}\rangle_{i,j}. \tag{30}$$

3.3. ***Temporal discretization.*** We apply the classical fourth-order Runge–Kutta method to integrate (30), which can be written in the form

$$\frac{d}{dt}\langle J\boldsymbol{U}\rangle_{i,j} = K(\langle J\boldsymbol{U}\rangle)_{i,j} \tag{31}$$

over grid cell $V_{i,j}$, where

$$K(\langle J\boldsymbol{U}\rangle)_{i,j} = -\frac{1}{\Delta\alpha}\left(\langle J\boldsymbol{F}^{\alpha}\rangle_{i+\frac{1}{2},j} - \langle J\boldsymbol{F}^{\alpha}\rangle_{i-\frac{1}{2},j}\right) - \frac{1}{\Delta\beta}\left(\langle J\boldsymbol{F}^{\beta}\rangle_{i,j+\frac{1}{2}} - \langle J\boldsymbol{F}^{\beta}\rangle_{i,j-\frac{1}{2}}\right) + \langle J\boldsymbol{\Psi}\rangle_{i,j}. \tag{32}$$

In Section 3.4, we show how to derive fourth-order accurate approximations to $K(\langle J\boldsymbol{U}\rangle)$ on grid cells given $\langle J\boldsymbol{U}\rangle$ on grid cells.

The classical Runge–Kutta method applied to the ordinary differential equation (31) integrated over time step Δt starting with $\langle J\boldsymbol{U}\rangle^{(0)}$ at the initial time is

$$k_1 = K(\langle J\boldsymbol{U}\rangle^{(0)})\Delta t, \tag{33}$$

$$\langle J\boldsymbol{U}\rangle^{(1)} = \langle J\boldsymbol{U}\rangle^{(0)} + \tfrac{1}{2}k_1, \qquad k_2 = K(\langle J\boldsymbol{U}\rangle^{(1)})\Delta t, \tag{34}$$

$$\langle J\boldsymbol{U}\rangle^{(2)} = \langle J\boldsymbol{U}\rangle^{(0)} + \tfrac{1}{2}k_2, \qquad k_3 = K(\langle J\boldsymbol{U}\rangle^{(2)})\Delta t, \tag{35}$$

$$\langle J\boldsymbol{U}\rangle^{(3)} = \langle J\boldsymbol{U}\rangle^{(0)} + k_3, \qquad k_4 = K(\langle J\boldsymbol{U}\rangle^{(3)})\Delta t. \tag{36}$$

Then to integrate one time step:

$$\langle J\boldsymbol{U}\rangle(t^n + \Delta t) = \langle J\boldsymbol{U}\rangle(t^n) + \tfrac{1}{6}(k_1 + 2k_2 + 2k_3 + k_4) + O((\Delta t)^5). \tag{37}$$

With local truncation error of $O((\Delta t)^5)$, as shown in (37), the accumulated error for the classical Runge–Kutta method is then $O((\Delta t)^4)$.

3.4. ***Spatial discretization.*** If Ω is the set of ordered pairs of indices (i, j) over which we find $\langle J\boldsymbol{U}\rangle_{i,j}$, then let $\mathcal{G}_{m,n}(\Omega)$, with m and n integers, be the set of grid cells Ω expanded by m layers of additional cells at both ends in the α direction and n layers of additional cells at both ends in the β direction. These additional cells are called *ghost cells*. For a set of indices Λ of grid cells and ghost cells, let $\mathcal{F}^{\alpha}(\Lambda)$ be the set of their faces of constant α and $\mathcal{F}^{\beta}(\Lambda)$ the set of their faces of constant β.

In the remainder of this section, we show how to compute the right-hand side of (30), the evolution equation for $\langle J\boldsymbol{U}\rangle$. The method is motivated by that in [32] for Cartesian grids, extended to mapped grids in [10] and to mapped multiblock grids in [31]. What is new here is that we are calculating on a 2D manifold in 3D and also that we have vector components that require a basis transformation (Step (2) below).

The discrete undivided-difference formulae denoted by D_{α} and D_{β} with various superscripts are defined in Appendix A.

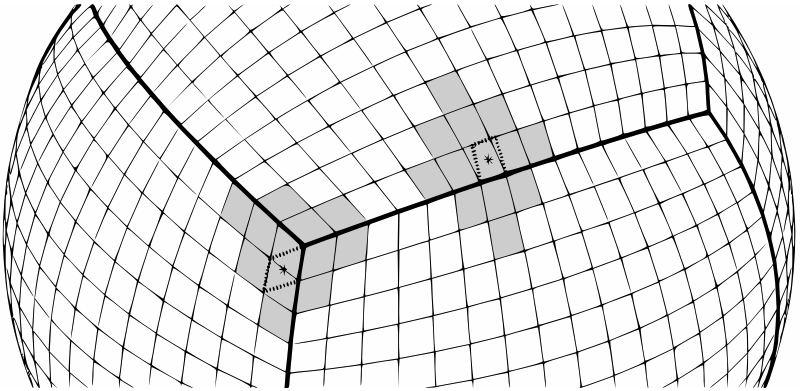

Figure 2. Sample interpolation stencils of two different ghost cells, used in Step (2). The procedure for finding the stencil is explained in [31]. The set of grid cells in the stencil is found as follows. First, find the center of the ghost cell on the cubed sphere, as marked with $*$ in this figure, and let $\boldsymbol{c}$ be the valid grid cell on a neighboring panel that contains that point. The stencil set then consists of all the valid cells sharing a vertex with $\boldsymbol{c}$ and also the cells two away from $\boldsymbol{c}$ in both directions along both coordinate dimensions, making the appropriate transformation when crossing a panel boundary.

(1) From $\langle \boldsymbol{JU} \rangle$ on Ω and $\langle J \rangle$ on $\mathcal{G}_{1,1}(\Omega)$, obtain $\langle \boldsymbol{U} \rangle$ on Ω by using (B-32), with adjustments at panel boundaries as described in Appendix B4. We then have $\langle \boldsymbol{U} \rangle$ accurate to fourth order in $\Delta\alpha = \Delta\beta$.

(2) Interpolate $\langle \boldsymbol{U} \rangle$ from Ω to the ghost cells $\mathcal{G}_{3,3}(\Omega) - \Omega$ by the method of least squares from stencils in [31]. See Figure 2 for an illustration of interpolation stencils for two sample ghost cells.

Once we find the set of stencil cells for a particular ghost cell, we rotate the entire sphere so that the center of the ghost cell lies on the equator. Let λ and ϕ denote the latitudinal and longitudinal displacements, respectively, of any point from the ghost cell's new center on the equator. For each stencil cell indexed by $\boldsymbol{s}$, let $\lambda_{\boldsymbol{s}}$ and $\phi_{\boldsymbol{s}}$ be the latitudinal and longitudinal displacements of its center from the rotated ghost-cell center. Define the stencil's average angular distance

$$\bar{\theta} = \frac{1}{N} \sum_{\boldsymbol{s}} \sqrt{\lambda_{\boldsymbol{s}}^2 + \phi_{\boldsymbol{s}}^2}, \tag{38}$$

where N is the number of stencil cells.

For the scalar component $\langle h \rangle$ of $\langle \boldsymbol{U} \rangle$, we follow the procedure in [31], approximating h by a Taylor polynomial over latitude and longitude and finding its coefficients a_{pq} for $p, q \geq 0$ and $p + q \leq 3$ satisfying as closely as possible the overdetermined system of N equations

$$\sum_{p,q \geq 0;\, p+q \leq 3} a_{pq} \left\langle \left(\frac{\lambda}{\bar{\theta}} \right)^p \left(\frac{\phi}{\bar{\theta}} \right)^q \right\rangle_{\boldsymbol{s}} = \langle h \rangle_{\boldsymbol{s}} \tag{39}$$

for all stencil cells $\boldsymbol{s}$, where the notation $\langle\cdot\rangle_{\boldsymbol{s}}$ represents averaging over cell $\boldsymbol{s}$ and (λ, ϕ) ranges over its values in cell $\boldsymbol{s}$. The system is overdetermined because there are 10 coefficients a_{pq} for which to solve and the number of equations, N, is either 12 or 13. (It is 12 only if the ghost cell is near the intersection of three panels.) We then evaluate the Taylor polynomial averaged over the ghost cell $\boldsymbol{g}$:

$$\langle h\rangle_{\boldsymbol{g}} = \sum_{p,q\ge 0;\, p+q\le 3} a_{pq}\left\langle \left(\frac{\lambda}{\bar{\theta}}\right)^p \left(\frac{\phi}{\bar{\theta}}\right)^q \right\rangle_{\boldsymbol{g}}. \tag{40}$$

The procedure above applies to the scalar component $\langle h\rangle$ of $\langle \boldsymbol{U}\rangle$, but $\langle \boldsymbol{U}\rangle$ also contains $\langle hu^\alpha\rangle$ and $\langle hu^\beta\rangle$, which are components in different bases in adjacent panels, so in order to find $\langle hu^\alpha\rangle$ and $\langle hu^\beta\rangle$ at the ghost cell, a basis transformation must be made.

At a point (λ, ϕ), let the basis-transformation matrix from a source panel $\mathcal{S}$, containing a stencil cell, to a destination panel $\mathcal{D}$, containing the ghost cell, be denoted

$$T_{\mathcal{S}\to\mathcal{D}}(\lambda,\phi) = \begin{pmatrix} T^{\alpha\alpha}_{\mathcal{S}\to\mathcal{D}}(\lambda,\phi) & T^{\alpha\beta}_{\mathcal{S}\to\mathcal{D}}(\lambda,\phi) \\ T^{\beta\alpha}_{\mathcal{S}\to\mathcal{D}}(\lambda,\phi) & T^{\beta\beta}_{\mathcal{S}\to\mathcal{D}}(\lambda,\phi) \end{pmatrix}.$$

Then our modification to (39)–(40) is to find coefficients b_{pq} and c_{pq} of two Taylor polynomials in the basis of the panel $\mathcal{P}(\boldsymbol{g})$ containing the ghost cell $\boldsymbol{g}$, satisfying as closely as possible the overdetermined system of $2N$ equations

$$\sum_{p,q\ge 0;\, p+q\le 3} b_{pq}\left\langle T^{\alpha\alpha}_{\mathcal{P}(\boldsymbol{s})\to\mathcal{P}(\boldsymbol{g})}(\lambda,\phi)\left(\frac{\lambda}{\bar{\theta}}\right)^p\left(\frac{\phi}{\bar{\theta}}\right)^q\right\rangle_{\boldsymbol{s}} + \sum_{p,q\ge 0;\, p+q\le 3} c_{pq}\left\langle T^{\alpha\beta}_{\mathcal{P}(\boldsymbol{s})\to\mathcal{P}(\boldsymbol{g})}(\lambda,\phi)\left(\frac{\lambda}{\bar{\theta}}\right)^p\left(\frac{\phi}{\bar{\theta}}\right)^q\right\rangle_{\boldsymbol{s}} = \langle hu^\alpha\rangle_{\boldsymbol{s}}, \tag{41}$$

$$\sum_{p,q\ge 0;\, p+q\le 3} b_{pq}\left\langle T^{\beta\alpha}_{\mathcal{P}(\boldsymbol{s})\to\mathcal{P}(\boldsymbol{g})}(\lambda,\phi)\left(\frac{\lambda}{\bar{\theta}}\right)^p\left(\frac{\phi}{\bar{\theta}}\right)^q\right\rangle_{\boldsymbol{s}} + \sum_{p,q\ge 0;\, p+q\le 3} c_{pq}\left\langle T^{\beta\beta}_{\mathcal{P}(\boldsymbol{s})\to\mathcal{P}(\boldsymbol{g})}(\lambda,\phi)\left(\frac{\lambda}{\bar{\theta}}\right)^p\left(\frac{\phi}{\bar{\theta}}\right)^q\right\rangle_{\boldsymbol{s}} = \langle hu^\beta\rangle_{\boldsymbol{s}} \tag{42}$$

for all stencil cells $\boldsymbol{s}$, where $\mathcal{P}(\boldsymbol{s})$ is the panel containing cell $\boldsymbol{s}$. Then we evaluate

$$\langle hu^\alpha\rangle_{\boldsymbol{g}} = \sum_{p,q\ge 0;\, p+q\le 3} b_{pq}\left\langle \left(\frac{\lambda}{\bar{\theta}}\right)^p \left(\frac{\phi}{\bar{\theta}}\right)^q \right\rangle_{\boldsymbol{g}}, \tag{43}$$

$$\langle hu^\beta\rangle_{\boldsymbol{g}} = \sum_{p,q\ge 0;\, p+q\le 3} c_{pq}\left\langle \left(\frac{\lambda}{\bar{\theta}}\right)^p \left(\frac{\phi}{\bar{\theta}}\right)^q \right\rangle_{\boldsymbol{g}}. \tag{44}$$

(3) On cells in $\mathcal{G}_{3,3}(\Omega)$, deconvolve from averages $\langle \boldsymbol{U} \rangle$ to $\boldsymbol{U}$ at centers by

$$\boldsymbol{U}_{i,j} = \langle \boldsymbol{U} \rangle_{i,j} - \tfrac{1}{24}(D_\alpha^{2c} \langle \boldsymbol{U} \rangle)_{i,j} - \tfrac{1}{24}(D_\beta^{2c} \langle \boldsymbol{U} \rangle)_{i,j} \quad \text{for } (i,j) \in \mathcal{G}_{2,2}(\Omega). \tag{45}$$

This formula is from (B-23) in Appendix B3 and is accurate to fourth order in $\Delta\alpha = \Delta\beta$.

(4) Obtain averages $\langle \boldsymbol{W} \rangle$ of primitive variables on $\mathcal{G}_{2,2}(\Omega)$ as follows. Set

$$\boldsymbol{W}_{i,j} = \boldsymbol{W}(\boldsymbol{U}_{i,j}) \qquad \text{for } (i,j) \in \mathcal{G}_{2,2}(\Omega), \tag{46}$$

$$\overline{\boldsymbol{W}}_{i,j} = \boldsymbol{W}(\langle \boldsymbol{U} \rangle_{i,j}) \quad \text{for } (i,j) \in \mathcal{G}_{3,3}(\Omega) \tag{47}$$

with $\boldsymbol{W}(\boldsymbol{U})$ being the pointwise function converting conserved variables to primitive variables. Then convolve:

$$\langle \boldsymbol{W} \rangle_{i,j} = \boldsymbol{W}_{i,j} + \tfrac{1}{24}(D_\alpha^{2c} \overline{\boldsymbol{W}})_{i,j} + \tfrac{1}{24}(D_\beta^{2c} \overline{\boldsymbol{W}})_{i,j} \quad \text{for } (i,j) \in \mathcal{G}_{2,2}(\Omega). \tag{48}$$

The result is accurate to fourth order in $\Delta\alpha = \Delta\beta$ because it uses (B-22) from Appendix B3, and $\overline{\boldsymbol{W}}_{i,j} - \boldsymbol{W}_{i,j}$ is second-order in $\Delta\alpha = \Delta\beta$. In (48), we apply the difference operators to $\overline{\boldsymbol{W}}$ instead of $\boldsymbol{W}$ to reduce the depth of ghost cells required, without dropping order.

(5) Interpolate $\langle \boldsymbol{W} \rangle$ from averages over grid cells and ghost cells to averages over faces, using the fourth-order-accurate formulae from [32]:

$$\langle \boldsymbol{W} \rangle_{i+\frac{1}{2},j} = \tfrac{7}{12}(\langle \boldsymbol{W} \rangle_{i,j} + \langle \boldsymbol{W} \rangle_{i+1,j}) - \tfrac{1}{12}(\langle \boldsymbol{W} \rangle_{i-1,j} + \langle \boldsymbol{W} \rangle_{i+2,j}) \quad \text{for } (i+\tfrac{1}{2}, j) \in \mathcal{F}^\alpha(\mathcal{G}_{0,1}(\Omega)), \tag{49}$$

$$\langle \boldsymbol{W} \rangle_{i,j+\frac{1}{2}} = \tfrac{7}{12}(\langle \boldsymbol{W} \rangle_{i,j} + \langle \boldsymbol{W} \rangle_{i,j+1}) - \tfrac{1}{12}(\langle \boldsymbol{W} \rangle_{i,j-1} + \langle \boldsymbol{W} \rangle_{i,j+2}) \quad \text{for } (i, j+\tfrac{1}{2}) \in \mathcal{F}^\beta(\mathcal{G}_{1,0}(\Omega)). \tag{50}$$

(6) Deconvolve from face-averaged $\langle \boldsymbol{W} \rangle$ to face-centered $\boldsymbol{W}$, using (B-27) to obtain $\boldsymbol{W}_{i+\frac{1}{2},j}$ for $(i+\frac{1}{2}, j) \in \mathcal{F}^\alpha(\Omega)$ and (B-29) to obtain $\boldsymbol{W}_{i,j+\frac{1}{2}}$ for $(i, j+\frac{1}{2}) \in \mathcal{F}^\beta(\Omega)$. These are fourth-order-accurate in $\Delta\alpha = \Delta\beta$.

(7) Set face-centered fluxes:

$$\boldsymbol{F}^\alpha_{i+\frac{1}{2},j} = \boldsymbol{F}(\boldsymbol{W}_{i+\frac{1}{2},j}) \qquad \text{for } (i+\tfrac{1}{2}, j) \in \mathcal{F}^\alpha(\Omega), \tag{51}$$

$$\overline{\boldsymbol{F}}^\alpha_{i+\frac{1}{2},j} = \boldsymbol{F}(\langle \boldsymbol{W} \rangle_{i+\frac{1}{2},j}) \quad \text{for } (i+\tfrac{1}{2}, j) \in \mathcal{F}^\alpha(\mathcal{G}_{0,1}(\Omega)), \tag{52}$$

$$\boldsymbol{F}^\beta_{i,j+\frac{1}{2}} = \boldsymbol{F}(\boldsymbol{W}_{i,j+\frac{1}{2}}) \qquad \text{for } (i, j+\tfrac{1}{2}) \in \mathcal{F}^\beta(\Omega), \tag{53}$$

$$\overline{\boldsymbol{F}}^\beta_{i,j+\frac{1}{2}} = \boldsymbol{F}(\langle \boldsymbol{W} \rangle_{i,j+\frac{1}{2}}) \quad \text{for } (i, j+\tfrac{1}{2}) \in \mathcal{F}^\beta(\mathcal{G}_{1,0}(\Omega)). \tag{54}$$

The difference $\boldsymbol{F}^\alpha_{i+\frac{1}{2},j} - \overline{\boldsymbol{F}}^\alpha_{i+\frac{1}{2},j}$ is second-order in $\Delta\alpha = \Delta\beta$ as is the difference $\boldsymbol{F}^\beta_{i,j+\frac{1}{2}} - \overline{\boldsymbol{F}}^\beta_{i,j+\frac{1}{2}}$.

(8) Convolve face-centered $\boldsymbol{F}^\alpha$ to obtain face averages $\langle \boldsymbol{F}^\alpha \rangle$ and convolve face-centered $\boldsymbol{F}^\beta$ to obtain face averages $\langle \boldsymbol{F}^\beta \rangle$ with the fourth-order accurate formulae

$$\langle \boldsymbol{F}^\alpha \rangle_{i+\frac{1}{2},j} = \boldsymbol{F}^\alpha_{i+\frac{1}{2},j} + \tfrac{1}{24}(D^{2\mathrm{f}}_\beta \bar{\boldsymbol{F}}^\alpha)_{i+\frac{1}{2},j} \quad \text{for } (i+\tfrac{1}{2}, j) \in \mathscr{F}^\alpha(\Omega), \tag{55}$$

$$\langle \boldsymbol{F}^\beta \rangle_{i,j+\frac{1}{2}} = \boldsymbol{F}^\beta_{i,j+\frac{1}{2}} + \tfrac{1}{24}(D^{2\mathrm{f}}_\alpha \bar{\boldsymbol{F}}^\beta)_{i,j+\frac{1}{2}} \quad \text{for } (i, j+\tfrac{1}{2}) \in \mathscr{F}^\beta(\Omega). \tag{56}$$

We take derivatives of $\bar{\boldsymbol{F}}$ instead of $\boldsymbol{F}$ in order to reduce the depth of ghost cells required. Since $\bar{\boldsymbol{F}}$ and $\boldsymbol{F}$ differ only by second order in $\Delta\alpha = \Delta\beta$, we see from (A-14) that including $\bar{\boldsymbol{F}}$ rather than $\boldsymbol{F}$ in (55)–(56) results in a difference in $\langle \boldsymbol{F}^\alpha \rangle_{i+\frac{1}{2},j}$ or $\langle \boldsymbol{F}^\beta \rangle_{i,j+\frac{1}{2}}$ that is fourth-order in $\Delta\alpha = \Delta\beta$.

(9) Add artificial dissipation: to smooth out oscillations due to the central difference operator, we add an artificial dissipation to the fluxes. The effect of this modification is a sixth-order diffusive operator, which retains the order of accuracy of the underlying scheme.

First set $v_{\max}$ to be the maximum wave speed over the whole domain, which for advection is the maximum of $r(|u^\alpha| + |u^\beta|)$ and for shallow-water equations is the maximum of $\sqrt{Gh} + r\max\{|u^\alpha|, |u^\beta|\}$, where h, u^α, and u^β are the components of $\boldsymbol{W}$. Then modify the fluxes with fifth undivided differences:

$$\langle \boldsymbol{F}^\alpha \rangle_{i+\frac{1}{2},j} = \langle \boldsymbol{F}^\alpha \rangle_{i+\frac{1}{2},j} - \gamma v_{\max}(D^{5\mathrm{f}}_\alpha \langle \boldsymbol{U} \rangle)_{i+\frac{1}{2},j} \quad \text{for } \mathscr{F}^\alpha(\Omega), \tag{57}$$

$$\langle \boldsymbol{F}^\beta \rangle_{i,j+\frac{1}{2}} = \langle \boldsymbol{F}^\beta \rangle_{i,j+\frac{1}{2}} - \gamma v_{\max}(D^{5\mathrm{f}}_\beta \langle \boldsymbol{U} \rangle)_{i,j+\frac{1}{2}} \quad \text{for } \mathscr{F}^\beta(\Omega), \tag{58}$$

where $\gamma = \frac{1}{128}$ for advection and $\gamma = \sqrt{2}/64$ for shallow-water equations. The coefficient γ has been chosen empirically so that the artificial dissipation is enough to smooth out oscillations but not so large as to detract from accuracy.

(10) Find the fourth-order convolution products

$$\langle J\boldsymbol{F}^\alpha \rangle_{i+\frac{1}{2},j} = \langle J \rangle_{i+\frac{1}{2},j} \langle \boldsymbol{F}^\alpha \rangle_{i+\frac{1}{2},j} + \tfrac{1}{12}(D^{1\mathrm{f}}_\beta \langle J \rangle)_{i+\frac{1}{2},j} (D^{1\mathrm{f}}_\beta \langle \bar{\boldsymbol{F}}^\alpha \rangle)_{i+\frac{1}{2},j} \quad \text{for } \mathscr{F}^\alpha(\Omega), \tag{59}$$

$$\langle J\boldsymbol{F}^\beta \rangle_{i,j+\frac{1}{2}} = \langle J \rangle_{i,j+\frac{1}{2}} \langle \boldsymbol{F}^\beta \rangle_{i,j+\frac{1}{2}} + \tfrac{1}{12}(D^{1\mathrm{f}}_\alpha \langle J \rangle)_{i,j+\frac{1}{2}} (D^{1\mathrm{f}}_\alpha \langle \bar{\boldsymbol{F}}^\beta \rangle)_{i,j+\frac{1}{2}} \quad \text{for } \mathscr{F}^\beta(\Omega). \tag{60}$$

We take differences of $\bar{\boldsymbol{F}}^\alpha$ and $\bar{\boldsymbol{F}}^\beta$ instead of $\langle \boldsymbol{F}^\alpha \rangle$ and $\langle \boldsymbol{F}^\beta \rangle$ in order to reduce the depth of ghost cells required, without dropping order. These approximations are fourth-order-accurate in $\Delta\alpha = \Delta\beta$.

(11) For each grid-cell face that is shared by two panels, after $\langle J\boldsymbol{F}^\alpha \rangle$ or $\langle J\boldsymbol{F}^\beta \rangle$ is computed on that face separately for each panel in Step (10), replace it by its average with the corresponding $\langle J\boldsymbol{F}^\alpha \rangle$ or $\langle J\boldsymbol{F}^\beta \rangle$ calculated on the same face in

the other panel that shares it. Note that $\langle J\boldsymbol{F}^{\alpha}\rangle$ or $\langle J\boldsymbol{F}^{\beta}\rangle$ from the other panel may need to be reoriented as follows:

- Faces that are shared with equatorial panels 2 or 4 and either of the polar panels, 5 or 6, have constant β on the equatorial panel and constant α on the polar panel; hence, on these faces, $\langle J\boldsymbol{F}^{\beta}\rangle$ on the equatorial panel is averaged with $\langle J\boldsymbol{F}^{\alpha}\rangle$ on the polar panel.
- Before averaging, sign changes are required for faces on the other panel along the following interfaces: $\langle J\boldsymbol{F}^{\beta}\rangle$ on Panel 2 with $\langle J\boldsymbol{F}^{\alpha}\rangle$ on Panel 5, $\langle J\boldsymbol{F}^{\beta}\rangle$ on Panel 4 with $\langle J\boldsymbol{F}^{\alpha}\rangle$ on Panel 6, and $\langle J\boldsymbol{F}^{\beta}\rangle$ on Panel 3 with $\langle J\boldsymbol{F}^{\beta}\rangle$ on either of the polar panels, 5 or 6.

For the vector fluxes, $\mathcal{T}^{\alpha k}$ and $\mathcal{T}^{\beta k}$, this is more complicated because the components are in different bases in different panels. Write

$$\Phi^{\alpha} = J\begin{pmatrix}\mathcal{T}^{\alpha\alpha}\\ \mathcal{T}^{\beta\alpha}\end{pmatrix} \quad \text{on faces of constant } \alpha, \tag{61}$$

$$\Phi^{\beta} = J\begin{pmatrix}\mathcal{T}^{\alpha\beta}\\ \mathcal{T}^{\beta\beta}\end{pmatrix} \quad \text{on faces of constant } \beta. \tag{62}$$

Then we set the following from (52), (54), and (59)–(60):

- $\langle\Phi^{\alpha}\rangle_{i+\frac{1}{2},j}$, vector components of $\langle J\boldsymbol{F}^{\alpha}\rangle_{i+\frac{1}{2},j}$, for $(i+\frac{1}{2}, j) \in \mathcal{F}^{\alpha}(\Omega)$,
- $\overline{\Phi}^{\alpha}_{i+\frac{1}{2},j}$, vector components of $J_{i+\frac{1}{2},j}\overline{\boldsymbol{F}}^{\alpha}_{i+\frac{1}{2},j}$, for $(i+\frac{1}{2}, j) \in \mathcal{F}^{\alpha}(\mathcal{G}_{0,1}(\Omega))$,
- $\langle\Phi^{\beta}\rangle_{i,j+\frac{1}{2}}$, vector components of $\langle J\boldsymbol{F}^{\beta}\rangle_{i,j+\frac{1}{2}}$, for $(i, j+\frac{1}{2}) \in \mathcal{F}^{\beta}(\Omega)$,
- $\overline{\Phi}^{\beta}_{i,j+\frac{1}{2}}$, vector components of $J_{i,j+\frac{1}{2}}\overline{\boldsymbol{F}}^{\beta}_{i,j+\frac{1}{2}}$, for $(i, j+\frac{1}{2}) \in \mathcal{F}^{\beta}(\mathcal{G}_{1,0}(\Omega))$.

We deconvolve to face centers

$$\Phi^{\alpha}_{i+\frac{1}{2},j} = \langle\Phi^{\alpha}\rangle_{i+\frac{1}{2},j} - \tfrac{1}{24}(D^{2\mathrm{f}}_{\beta}\overline{\Phi}^{\alpha})_{i+\frac{1}{2},j} \quad \text{for } (i+\tfrac{1}{2}, j) \in \mathcal{F}^{\alpha}(\Omega), \tag{63}$$

$$\Phi^{\beta}_{i,j+\frac{1}{2}} = \langle\Phi^{\beta}\rangle_{i,j+\frac{1}{2}} - \tfrac{1}{24}(D^{2\mathrm{f}}_{\alpha}\overline{\Phi}^{\beta})_{i,j+\frac{1}{2}} \quad \text{for } (i, j+\tfrac{1}{2}) \in \mathcal{F}^{\beta}(\Omega) \tag{64}$$

and convert to the orthonormal frame with orthonormalization matrices $\mathbb{O}^{\alpha}_{i+\frac{1}{2},j}$ and $\mathbb{O}^{\beta}_{i,j+\frac{1}{2}}$ (see [56]) at face centers:

$$\Theta^{\alpha}_{i+\frac{1}{2},j} = \mathbb{O}^{\alpha}_{i+\frac{1}{2},j}\Phi^{\alpha}_{i+\frac{1}{2},j} \quad \text{for } (i+\tfrac{1}{2}, j) \in \mathcal{F}^{\alpha}(\Omega), \tag{65}$$

$$\Theta^{\beta}_{i,j+\frac{1}{2}} = \mathbb{O}^{\beta}_{i,j+\frac{1}{2}}\Phi^{\beta}_{i,j+\frac{1}{2}} \quad \text{for } (i, j+\tfrac{1}{2}) \in \mathcal{F}^{\beta}(\Omega), \tag{66}$$

$$\overline{\Theta}^{\alpha}_{i+\frac{1}{2},j} = \mathbb{O}^{\alpha}_{i+\frac{1}{2},j}\overline{\Phi}^{\alpha}_{i+\frac{1}{2},j} \quad \text{for } (i+\tfrac{1}{2}, j) \in \mathcal{F}^{\alpha}(\mathcal{G}_{0,1}(\Omega)), \tag{67}$$

$$\overline{\Theta}^{\beta}_{i,j+\frac{1}{2}} = \mathbb{O}^{\beta}_{i,j+\frac{1}{2}}\overline{\Phi}^{\beta}_{i,j+\frac{1}{2}} \quad \text{for } (i, j+\tfrac{1}{2}) \in \mathcal{F}^{\beta}(\mathcal{G}_{1,0}(\Omega)). \tag{68}$$

On each face of a panel boundary, we replace each of Θ^α and $\overline{\Theta}^\alpha$, or each of Θ^β and $\overline{\Theta}^\beta$, with the averages from the two panels sharing that face. In the case of faces shared by either Panel 2 or 4 and either Panel 5 or 6, we flip the sign of the quantity from the opposite panel before averaging.

Finally, we set the vector components of $\langle J\boldsymbol{F}^\alpha\rangle_{i+\frac{1}{2},j}$ and $\langle J\boldsymbol{F}^\beta\rangle_{i,j+\frac{1}{2}}$ to

$$\langle\widetilde{\Phi}^\alpha\rangle_{i+\frac{1}{2},j} = (\mathbb{O}^\alpha_{i+\frac{1}{2},j})^{-1}\Theta^\alpha_{i+\frac{1}{2},j} + \tfrac{1}{24}(D^{2\mathrm{f}}_\beta((\mathbb{O}^\alpha)^{-1}\overline{\Theta}^\alpha))_{i+\frac{1}{2},j} \quad \text{for } (i+\tfrac{1}{2}, j) \in \mathscr{F}^\alpha(\Omega), \quad (69)$$

$$\langle\widetilde{\Phi}^\beta\rangle_{i,j+\frac{1}{2}} = (\mathbb{O}^\beta_{i,j+\frac{1}{2}})^{-1}\Theta^\beta_{i,j+\frac{1}{2}} + \tfrac{1}{24}(D^{2\mathrm{f}}_\beta((\mathbb{O}^\beta)^{-1}\overline{\Theta}^\beta))_{i,j+\frac{1}{2}} \quad \text{for } (i, j+\tfrac{1}{2}) \in \mathscr{F}^\beta(\Omega). \quad (70)$$

Now for $(i, j) \in \Omega$, we have fourth-order-accurate $\langle J\boldsymbol{F}^\alpha\rangle_{i\pm\frac{1}{2},j}$ and $\langle J\boldsymbol{F}^\beta\rangle_{i,j\pm\frac{1}{2}}$ on the right-hand side of (30), the evolution equation for $\langle J\boldsymbol{U}\rangle_{i,j}$.

The source term $\langle J\boldsymbol{\Psi}\rangle_{i,j}$ in (30) is computed as follows. From (46), we have $\boldsymbol{W}_{i,j}$ on centers of grid cells $(i, j) \in \mathscr{G}_{2,2}(\Omega)$. Since $\boldsymbol{\Psi}$ is a function of $\boldsymbol{W}$, we can find $\boldsymbol{\Psi}_{i,j}$ for $(i, j) \in \mathscr{G}_{1,1}(\Omega)$, multiply it by $J_{i,j}$, and apply the convolution formula (B-22) to find the averaged $\langle J\boldsymbol{\Psi}\rangle_{i,j}$ for $(i, j) \in \Omega$ to fourth-order accuracy.

4. Adaptive mesh refinement

With adaptive mesh refinement (AMR), we extend the approach of [19] on single-block mapped grids to the mapped-multiblock grids of the cubed sphere. What makes the cubed sphere different from single-block mapped grids is that the solution is on a manifold, we are able to use analytic formulae for integrals of $\langle J\rangle$, and adjacent panels have different mappings.

To implement adaptive mesh refinement, we make use of the Chombo library for parallel AMR [1] and follow the strategies used therein. Adaptive-mesh-refinement calculations are performed on a hierarchy of nested meshes $\Omega^\ell \subset \Gamma^\ell$, with $\Omega^\ell \supset \mathscr{C}_{n^\ell_{\mathrm{ref}}}(\Omega^{\ell+1})$ where n^ℓ_{ref} denotes the refinement ratio between levels ℓ and $\ell+1$ and $\mathscr{C}_{n^\ell_{\mathrm{ref}}}$ denotes coarsening by this ratio. At level ℓ, we label all cells inside Ω^ℓ as being valid and all cells outside Ω^ℓ (such as ghost cells) as being invalid. Typically, Ω^ℓ is decomposed into a disjoint union of rectangles in order to perform calculations efficiently. We assume that there are a sufficient number of cells on level ℓ separating the level-$(\ell+1)$ cells from the level-$(\ell-1)$ cells such that interpolations to fill invalid ghost cells on finer levels can be independently performed. We will refer to grid hierarchies that meet this condition as being *properly nested*.

The top-level procedure for advancing level ℓ from time t^ℓ by a time step of length Δt^ℓ is shown in Figure 3.

Advance$(\ell, t^\ell, \Delta t^\ell)$:

(1) Regrid levels finer than ℓ if required (see Section 4.1).

(2) Advance level ℓ using the methods described in Section 3 with a Runge–Kutta time-stepping method.

(3) Interpolate to the invalid ghost cells surrounding level $\ell+1$ (see Section 4.2). A least-squares algorithm is used to compute the interpolating polynomial in each coarse cell. The interpolation need not be conservative because the resulting values in the ghost cells are only used to reconstruct the flux on the faces of the valid cells.

(4) Start level $\ell+1$ at Step (1). Level $\ell+1$ is refined in time (subcycled) with a time step $\Delta t^{\ell+1} = \Delta t^\ell / n^\ell_{\text{ref}}$.

(5) Average the solution from level $\ell+1$ and correct fluxes at coarse-fine interfaces to ensure conservation.

Figure 3. Pseudocode for advancing level ℓ from time t^ℓ to time $t^\ell + \Delta t^\ell$.

4.1. ***Regridding.*** Periodically, it is necessary to change the grid hierarchy in response to changes in the solution. During a regrid, we generate a new grid hierarchy, $\{\Omega^{\ell,\text{new}}\}_{\ell=\ell_{\text{base}}+1,\ldots,\ell_{\max}}$ leaving the mesh at ℓ_{base} and all coarser levels unchanged.

For $\ell = \ell_{\text{base}}, \ldots, \ell^{\text{new}}_{\max} - 1$, we use a least-squares algorithm to interpolate ghost values. For each ghost cell $V_{i,j}$, let $\mathcal{I}(i,j)$ denote the set of grid cells of its interpolation stencil. We solve a least-squares system for the coefficients $a^{i,j}_{p,q}$ of a polynomial interpolant of $\boldsymbol{U}$,

$$\sum_{p\geq 0; q\geq 0; p+q\leq 3} a^{i,j}_{p,q} \langle \alpha^p \beta^q \rangle_{i',j'} = \langle \boldsymbol{U} \rangle_{i',j'} \quad \text{for all } (i',j') \in \mathcal{I}(i,j) \tag{71}$$

(where α^p and β^q indicate powers of α and β), subject to a conservation constraint on $J\boldsymbol{U}$,

$$\sum_{(i',j')\in \mathcal{C}^{-1}(\{(i,j)\})} \; \sum_{p\geq 0; q\geq 0; p+q\leq 3} a^{i,j}_{p,q} \langle J\alpha^p \beta^q \rangle_{i',j'} = \langle J\boldsymbol{U} \rangle_{i,j}. \tag{72}$$

The moments $\langle \alpha^p \beta^q \rangle$ can be determined analytically, and the $\langle J\alpha^p \beta^q \rangle$ are computed using the product formula. Given this interpolant, we can construct $\langle J\boldsymbol{U} \rangle$ on the grid cells at level $\ell+1$ within $V_{i,j}$:

$$\langle J\boldsymbol{U} \rangle_{i',j'} = \sum_{p\geq 0; q\geq 0; p+q\leq 3} a^{i,j}_{p,q} \langle J\alpha^p \beta^q \rangle_{i',j'} \quad \text{for all } (i',j') \in \mathcal{C}^{-1}(\{(i,j)\}). \tag{73}$$

This interpolation is conservative.

4.2. ***Interpolating to ghost cells at next finer level.*** As shown in Section 3.4, advancing one time step by the method of Section 3 requires three layers of ghost cells. In Step (3) of the algorithm of Figure 3, we must interpolate $\langle J\boldsymbol{U}\rangle$ from level ℓ to the ghost cells of level $\ell+1$. In particular, after Step (2) of **Advance**$(\ell, t^\ell, \Delta t^\ell)$ advances the solution at level ℓ from time t^ℓ to time $t^\ell+\Delta t^\ell$, Step (3) interpolates the level-ℓ solution to ghost cells of level $\ell+1$ at times $t^\ell+s\Delta t^{\ell+1}$ for $s=0,\dots,n_{\text{ref}}^\ell-1$, where $\Delta t^{\ell+1}=\Delta t^\ell/n_{\text{ref}}^\ell$ is the length of the time step at level $\ell+1$. Step (3) has the following substeps:

(a) Interpolate $\langle J\boldsymbol{U}\rangle$ on grid cells of level ℓ to the same grid cells at the intermediate times $t^\ell+s\Delta t^{\ell+1}$ for $s=1,\dots,n_{\text{ref}}^\ell-1$. This temporal interpolation uses initial $\langle J\boldsymbol{U}\rangle^{(0)}=\langle J\boldsymbol{U}\rangle(t^\ell)$ and k_1, k_2, k_3, and k_4 in the Runge–Kutta method defined in (33)–(36) in Section 3.3. As derived in [20], for $0\le\chi\le1$, we have

$$\langle J\boldsymbol{U}\rangle(t^\ell+\chi\Delta t^\ell)=\langle J\boldsymbol{U}\rangle(t^\ell)+\chi k_1+\tfrac{1}{2}\chi^2(-3k_1+2k_2+2k_3-k_4)+\tfrac{2}{3}\chi^3(k_1-k_2-k_3+k_4)+O((\Delta t^\ell)^4). \quad (74)$$

(b) At each of the times $t^\ell+s\Delta t^{\ell+1}$ for $s=0,\dots,n_{\text{ref}}^\ell-1$, fill in $\lceil(L+2)/n_{\text{ref}}^\ell\rceil$ layers of extrapanel ghost cells of $\langle J\boldsymbol{U}\rangle$ at level ℓ, by the method of least squares using interpolation stencils, described in Step (2) of Section 3.4.

(c) Fill in ghost cells of level $\ell+1$, by least-squares interpolation from the valid cells and ghost cells at level ℓ.

The temporal interpolation in Step (a) is the same as in [32]. With error of $O((\Delta t^\ell)^4)$, this interpolation preserves the order of the Runge–Kutta temporal discretization of Section 3.3. The spatial interpolation of Steps (b)–(c) is also fourth-order in the grid spacing.

5. Numerical tests

The Courant–Friedrichs–Lewy (CFL) number is

$$\frac{\Delta t}{\Delta\alpha}c_{\max}, \quad (75)$$

where Δt is the time step and $c_{\max}$ is the maximum wave speed.

As shown in [10], the stability constraint for the classical Runge–Kutta method we use is that the CFL number satisfy

$$\frac{\Delta t}{\Delta\alpha}c_{\max}\lesssim 2.06. \quad (76)$$

For advection, $c_{\max}$ is the maximum over the domain of $r(|u^\alpha|+|u^\beta|)$. For shallow-water equations, $c_{\max}$ is the maximum over the domain of the characteristic velocity $2\sqrt{Gh}+r(|u^\alpha|+|u^\beta|)$.

We note that the results presented here are for a method that does not employ any limiters or nonlinear filters that would suppress oscillations at discontinuities. We have constructed limiters for the Cartesian versions of the method in [32; 6]. While the extension of the approach used in that work to the present setting is straightforward, we have chosen not to apply it here, in order to obtain a clean assessment of the properties of the basic high-order method. There is a separate issue regarding positivity preservation, which historically has been an additional goal in the design of limiters. Our thinking on this issue is that the use of limiters for positivity preservation is an excessive constraint on the design choices in the method. Typically, a limiter can be thought of as a nonlinear hybridization of low- and high-order fluxes. To obtain a positivity-preserving limiter, it is a necessary condition for the low-order method to be positivity-preserving. For the case of advection, it is easy to construct a combination of a discretely divergence-free velocity field and a density distribution such that the only positivity-preserving field is donor-cell plus an explicit diffusion, which has a CFL time-step constraint that scales with the inverse of the dimensionality of the problem. Such a time-step constraint is stricter than that of the high-order methods of the type described here, even in 3D. For that reason, we are pursuing a different approach to positivity preservation based on redistribution of mass as a postprocessing step at the end of each time step [22]. Such an approach greatly expands the design space of limiter-based methods; for a discussion, see [6].

5.1. ***Deformational flow.*** To test the performance of the model under horizontal tracer transport, the deformational flow test [34, Test 4] is employed. This test is significantly more challenging than the solid-body rotation test of [61] since it not only tests divergent-free advection but also includes deformational stretching and the formation of thin filaments in the tracer field followed by subsequent recovery of the original profile. To obtain an analytical reference solution, the deformational-flow test reverses the time-varying flow field after half the total simulation period. The availability of an analytical reference solution at the final time means that error norms can be easily computed. Further, the addition of a solid-body rotation component to the flow field prevents the possible cancellation of errors when the flow is reversed.

In the transport equation (20) for h, the longitudinal component u_λ and latitudinal component u_ϕ of the flow field $\boldsymbol{u}$ take the form

$$u_\lambda = k \sin^2(\lambda') \sin(2\phi) \cos\left(\frac{\pi t}{T}\right) + \frac{2\pi}{T} \cos\phi, \tag{77}$$

$$u_\phi = k \sin(2\lambda') \cos\phi \cos\left(\frac{\pi t}{T}\right), \tag{78}$$

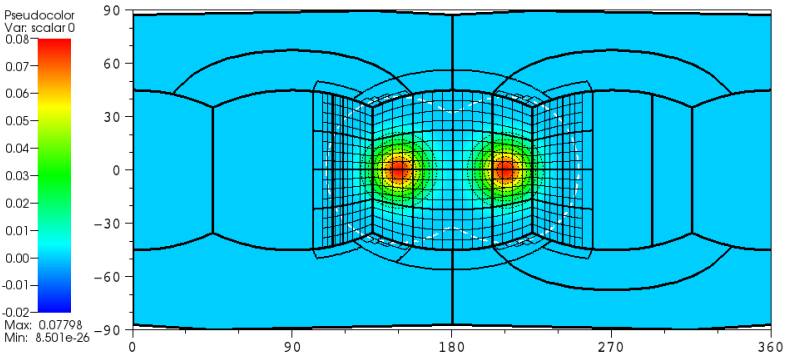

Figure 4. Plot of h at initial time in the deformational-flow test example of Section 5.1, with grids of resolutions c32/c128/c512. At this time, there is 34.4% c128 coverage and 27.9% c512 coverage. A dashed white contour line is drawn for h at the common refinement threshold of 5×10^{-5}, and dotted black contour lines are drawn at values of the positive tick marks in the legend.

where $\lambda' = \lambda - 2\pi t/T$, $k = 2$, $T = 5$ days, and $k = 2$. The height field consists of two superimposed smooth 2D Gaussian surfaces,

$$h(\lambda, \phi) = \sum_{i \in \{1,2\}} h_i(\lambda, \phi), \tag{79}$$

$$h_i(\lambda, \phi) = h_{\max} \exp\{-b_0 \delta_{\mathrm{xyz}}(\lambda, \phi; \lambda_i, \phi_i)\}, \tag{80}$$

where $i \in \{1, 2\}$, $h_{\max} = 1$, $b_0 = 10$, and $\delta_{\mathrm{xyz}}(\lambda, \phi; \lambda_i, \phi_i)$ is the 3D absolute Cartesian distance between (λ, ϕ) and (λ_i, ϕ_i) on the unit sphere,

$$\delta_{\mathrm{xyz}}(\lambda, \phi; \lambda_i, \phi_i) = \big[(\cos\phi \cos\lambda - \cos\phi_i \cos\lambda_i)^2 + (\cos\phi \sin\lambda - \cos\phi_i \sin\lambda_i)^2 + (\sin\phi - \sin\phi_i)^2\big]^{1/2}. \tag{81}$$

The centers of the Gaussian surfaces are located at $(\lambda_1, \phi_1) = (5\pi/6, 0)$ and $(\lambda_2, \phi_2) = (7\pi/6, 0)$. Although [34] has the setting $b_0 = 5$, here we instead set $b_0 = 10$ to narrow the width of the Gaussian surfaces, in order to highlight the benefits of AMR.

We run this example with the following resolutions:

- uniform resolution, with N_c a power of 2 from 32 through 1024,
- on two levels, the coarser level N_c a power of 2 from 32 through 256 and the finer level consisting of grids that are a factor of 4 finer and are located in regions where $|h| \geq 8 \times 10^{-4}/(N_c/64)^4$, and
- on three levels, the coarsest level N_c either 32 or 64, the middle level consisting of grids that are a factor of 4 finer and are located in regions where $|h| \geq 8 \times 10^{-4}/(N_c/16)^4$, and the finest level consisting of grids that are a factor of 4 finer than the middle-level grids and are located in the same regions.

Finest resolution	Uniform resolution max error	rate	Two levels max error	rate	Three levels max error	rate
c32	4.003×10^{-2}					
		0.88				
c64	2.162×10^{-2}					
		1.73				
c128	6.527×10^{-3}		6.544×10^{-3}			
		3.33		3.33		
c256	6.507×10^{-4}		6.506×10^{-4}			
		3.97		3.97		
c512	4.150×10^{-5}		4.150×10^{-5}		4.150×10^{-5}	
		4.00		4.00		4.00
c1024	2.586×10^{-6}		2.586×10^{-6}		2.586×10^{-6}	

Table 2. Maximum solution error at the final time, and convergence rates, for the deformational-flow test example of Section 5.1. When there is more than one level, the refinement ratio between consecutive levels is set to 4. Hence, in the two-level runs with results given here, where the finer levels are c128 through c1024, the coarser level is c32 through c256. Of the three-level runs, the first one has the refinements of the levels as c32/c128/c512 and the second has c64/256/c1024.

Figure 4 shows a plot of h at the initial time. The refinement thresholds have been selected to be comparable to the predicted asymptotically fourth-order solution error. We pick time step $\Delta t = 0.4\,\text{day}/N_c$, and we find $c_{\max} = 5.99\,\text{rad/day}$, so the CFL number from (75) is 1.53.

Table 2 shows the maximum solution error for each of the different runs. This table also shows the convergence rate of the maximum solution error, computed from two successively finer resolutions: since each successive resolution is refined by a factor of 2, this rate is the base-2 logarithm of the ratio of the errors. We see that the solution error converges to fourth order, and the error in each multilevel run is as good as that in the single-level run with the resolution of the finest level, with the level refinement criteria we use. Since the refinement criteria are such that finer grids are added where h is above a certain threshold, this example is not necessarily good for showing convergence at refinement boundaries, and so in Section 5.4, we show results of an example with fixed grids.

For the three simulations of deformational flow with coarsest level c32, Figure 5 shows plots of the error in h at the final time, where the maximum errors are the numbers shown in the first rows of the columns of Table 2. For these same three simulations, Figure 6 shows plots of h at the midpoint in time.

Figure 7 shows the fraction of the domains covered by finer-level grids during the multilevel simulations. Owing to the pattern of deformational flow, domain coverage of refined levels is highest near the midpoint in time and, in our runs, reaches its maximum of 68.2% for coverage of c128 in the c32/c128/c512 run. Because the refinement thresholds are equal, the coverage of c512 is almost the same in the c128/c512 and c32/c128/c512 runs. For the same reason, the coverage of c1024 is almost the same in the c256/c1024 and c64/c256/c1024 runs.

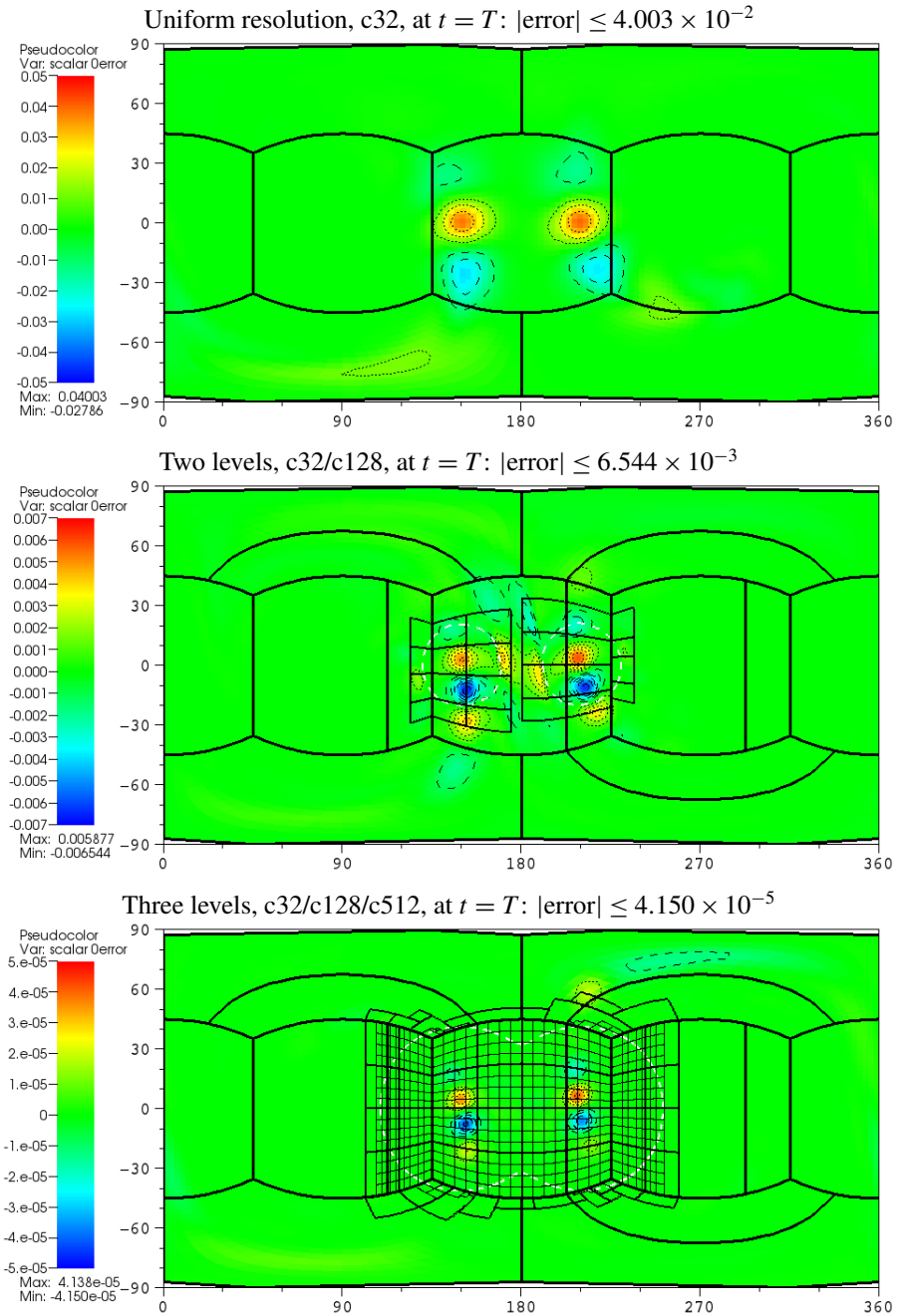

Figure 5. Plots of the error in h at the final time in the deformational-flow test example of Section 5.1, with c32 at the coarsest level. Grids at all levels at this time are shown. Black contour lines are drawn at values of the tick marks in the legend: dotted for positive and dashed for negative. For the two-level and three-level runs, dashed white contour lines are drawn at the refinement threshold for the calculated h at this time.

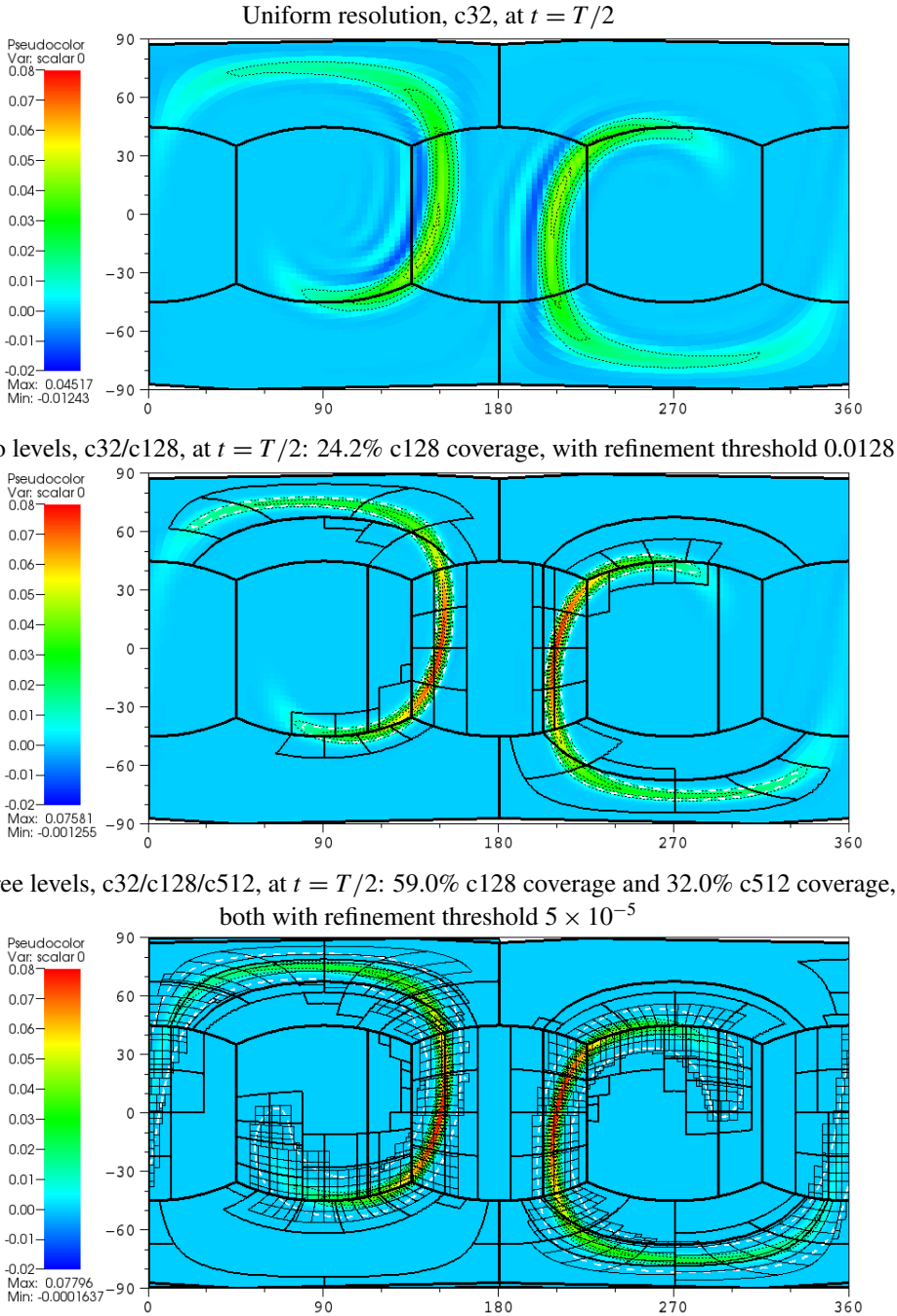

Figure 6. Plot of h at the midpoint in time, $t = T/2$, in the deformational-flow test example of Section 5.1, with c32 at the coarsest level. Grids at all levels at this time are shown. Dotted black contour lines are drawn at values of the positive tick marks in the legend, and in the two multilevel runs, dashed white contour lines are drawn at the refinement threshold.

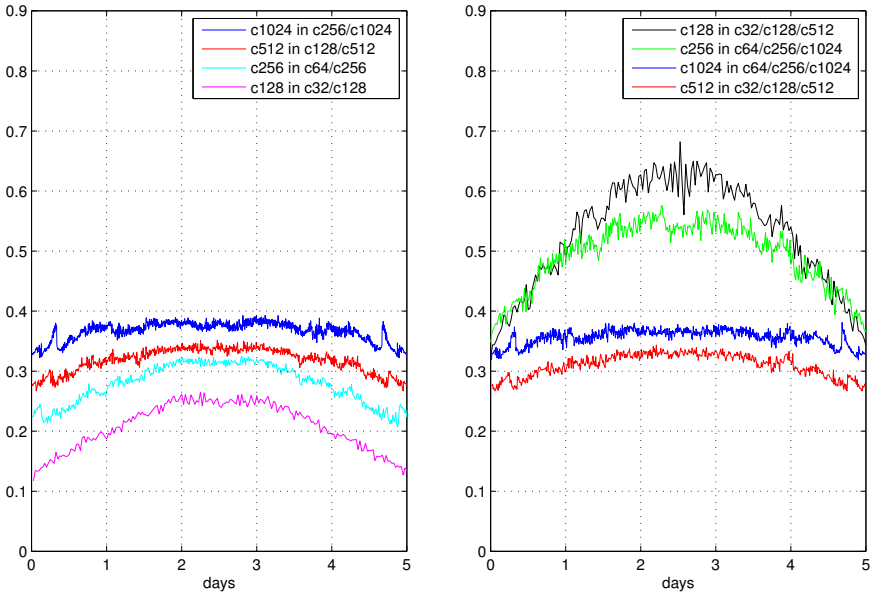

Figure 7. Plot of domain coverage of finer levels over time in the deformational-flow test of Section 5.1. Left: coverage of the finer level in two-level runs. Coverage increases with greater resolution because the refinement threshold is proportional to the fourth power of the grid spacing at the coarser level. Right: coverage of the middle and finest levels in three-level runs. As indicated by the red and dark-blue curves, coverage of the finest level in each three-level run matches coverage of the finer level in the two-level run with the same finest-level resolution because the refinement threshold is the same. In each three-level run, coverage of the middle level (black and green curves) is necessarily higher than coverage of the finest level (dark-blue and red curves) because proper-nesting conditions must be maintained. The gap between each three-level run's middle-level and finest-level coverage shrinks as resolution increases because proper-nesting conditions are expressed in terms of number of grid cells and grid cells become smaller with finer resolution.

5.2. ***Barotropically unstable jet without initial perturbation.*** The barotropic-instability test case of [15] consists of a zonal jet with compact support at a latitude of 45°. As in [24; 60], we first show the results of this test *without* the initial height perturbation that initiates the instability because we can check the order of accuracy of our method by comparing with the exact steady-state solution.

We pick time step $\Delta t = 0.25\,\text{day}/N_c$, and we find $c_{\max} = 10.1\text{rad/day}$, so the CFL number from (75) is 1.61. We run this example up to day 5 with the following resolutions:

- uniform resolution, with N_c a power of 2, from 16 through 1024,
- on two levels, the coarser level N_c a power of 2 from 16 through 256 and the finer level consisting of grids that are a factor of 4 finer and are located in regions where relative vorticity exceeds $0.32/\pi\ \text{day}^{-1} = 0.102\,\text{day}^{-1}$, and

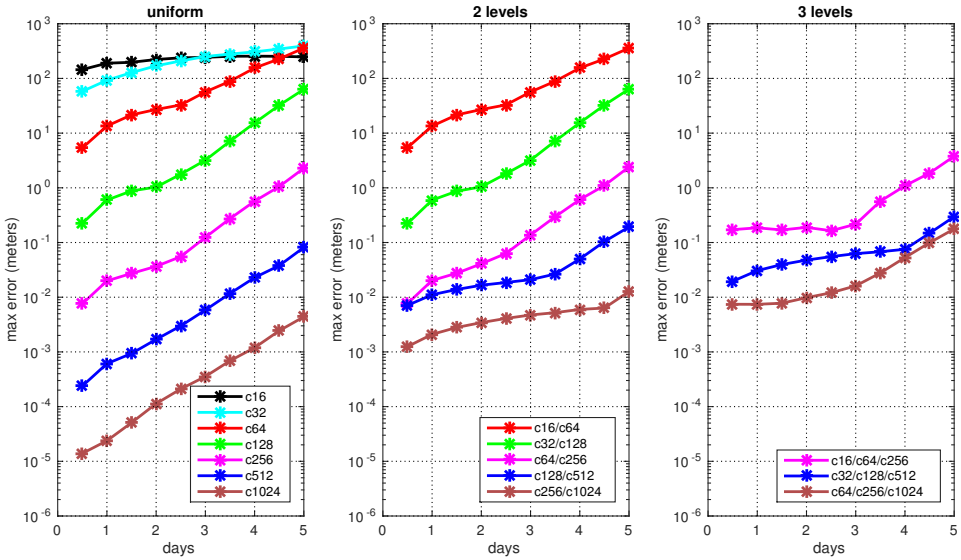

Figure 8. Plots of maximum error in height for the example in Section 5.2 of the steady-state (but unstable) jet of [15] without the initial perturbation, shown at intervals of every half day. Plots for runs with the same *finest*-level resolution have the same color.

- on three levels, the coarsest level N_c a power of 2 from 16 through 64, the middle level consisting of grids that are a factor of 4 finer and are located in regions where relative vorticity exceeds $0.32/\pi$ day$^{-1} = 0.102$ day^{-1}, and the finest level consisting of grids that are a factor of 4 finer than the middle-level grids and are located in regions where relative vorticity exceeds $1.28/\pi$ day$^{-1} = 0.407$ day^{-1}.

Figure 8 shows the maximum error in height for this example. We find that on uniform grids (left plot), the error is approximately fourth-order in the spatial resolution for c128 and finer; at coarser resolutions, the barotropic jet is not resolved, leading to a loss of convergence. For the two-level runs (center plot), the curves of maximum error over time match those of the finer level with uniform resolution for c16/c64, c32/c128, and c64/c256; but with more grid resolution, the two-level error is higher because the refinement threshold is too high to resolve it. For the three-level runs (right plot), the maximum error for c16/c64/c256 is a little higher than that for c64/c256 after day 3, and the maximum error for c32/c128/c512 is a little higher than that for c128/c512 after day 4, but the maximum errors at earlier times are higher because of the refinement threshold.

5.3. ***Barotropic instability.*** In the barotropic-instability test case of [15], a small height perturbation is added atop the jet, which leads to the controlled formation of an instability in the flow. The relative vorticity of the flow field at day 6 can then

be visually compared against a high-resolution numerically computed solution [15; 49]. For comparison, we use the simulation without additional explicit diffusion since the additional diffusion suggested in [15] leads to a significantly different flow field.

As in Section 5.2, we pick time step $\Delta t = 0.25\,\text{day}/N_c$. We now find $c_{\max} = 10.4\,\text{rad/day}$, so the CFL number from (75) is 1.66. We run this example up to day 6 with the same resolutions and refinement criteria as in Section 5.2. In the absence of an exact solution, we compare with the uniform c1024 solution as a reference.

Figure 9 shows the relative vorticity field at the final time for uniform c32, two-level c32/c128, and three-level c32/c128/c512. As shown in this figure, features are not sufficiently resolved on uniform c32, but the addition of a finer level refined by a factor of 4 improves the resolution in the region of instability (c32/c128), and resolution is further improved with the addition of a third level (c32/c128/c512).

Figure 10, on the top half, shows the maximum difference in relative vorticity between uniform c1024 and each other run at half-day intervals. Above the refinement threshold of $0.102\,\text{day}^{-1}$, curves of maximum difference with c1024 look approximately the same when the finest level has the same resolution. Specifically, the result for two-level c16/c64 matches that for uniform c64, c32/c128 matches uniform c128, c64/c256 and c16/c64/c256 match uniform c256, and c128/c512 and c32/c128/c512 match uniform c512 above the refinement threshold of $0.102\,\text{day}^{-1}$. The bottom half of Figure 10 shows the maximum difference in relative vorticity between each two-level and three-level run and the corresponding run having uniform resolution of the finest level; this difference stays below the refinement threshold until approximately day 5, when the instability is fully formed.

Total energy E is invariant under the shallow-water equations and is defined by

$$E = \tfrac{1}{2} h\boldsymbol{u}\cdot\boldsymbol{u} + \tfrac{1}{2} G(H^2 - z_s^2). \tag{82}$$

We calculate total energy by an area-weighted sum over the whole domain, accurate up to $O((\Delta\alpha)^2) = O((\Delta\beta)^2)$. In regions covered by grids with multiple levels of refinement, we take the sum over the finest level. Figure 11 shows the difference in total energy over time from its initial value, normalized by the initial total energy, for several runs: uniform c32, c128, and c512, two-level c32/c128, and three-level c32/c128/c512. We observe that higher spatial resolution corresponds to a substantial decrease in energy loss to numerical diffusion, with spatial convergence occurring at roughly fourth-order accuracy up to about day 4. At the highest resolutions, the calculation of total integrated shallow-water energy is dominated by truncation errors, leading to highly oscillatory behavior during the early part of the simulation. Results for the two-level c32/c128 and especially the three-level c32/c128/c512 are even more oscillatory because refinement does not necessarily preserve total energy. Nonetheless, all the simulations show a positive mean energy

Uniform resolution, c32

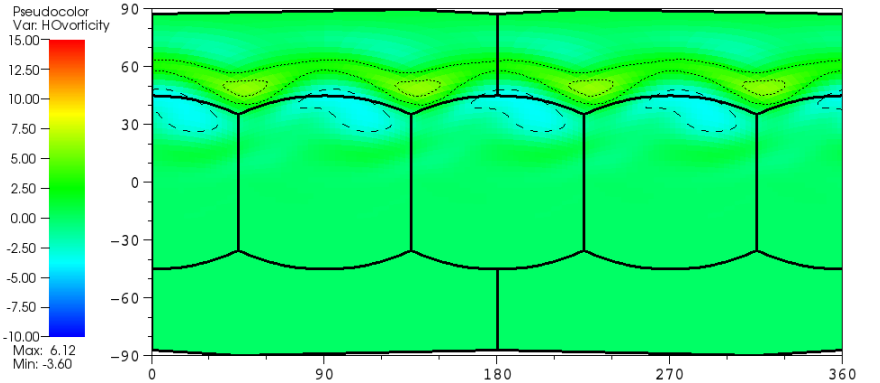

Two levels, c32/c128: 54.2% c128 coverage, with refinement threshold 0.102 day^{-1}

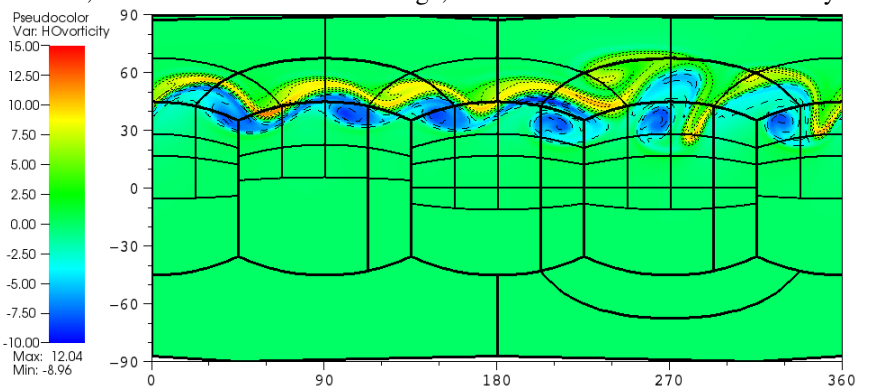

Three levels, c32/c128/c512: 54.2% c128 coverage, with refinement threshold 0.102 day^{-1}, and 32.9% c512 coverage, with refinement threshold 0.407 day^{-1}

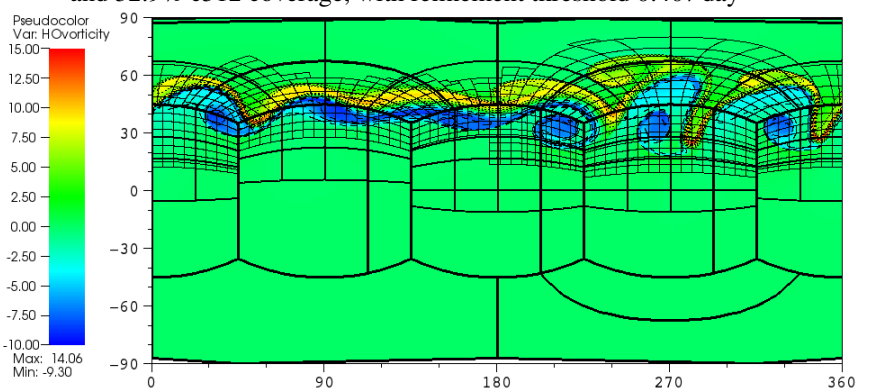

Figure 9. Relative vorticity field (in units of day^{-1}) at the final time (6 days) in the barotropic-instability test of Section 5.3, for c32 at the coarsest level. Black contour lines are drawn at values of the tick marks in the legend: dotted for positive and dashed for negative. In the two-level and three-level cases shown here, the second-level grids are the same and cover an area that coincides approximately with the northern hemisphere.

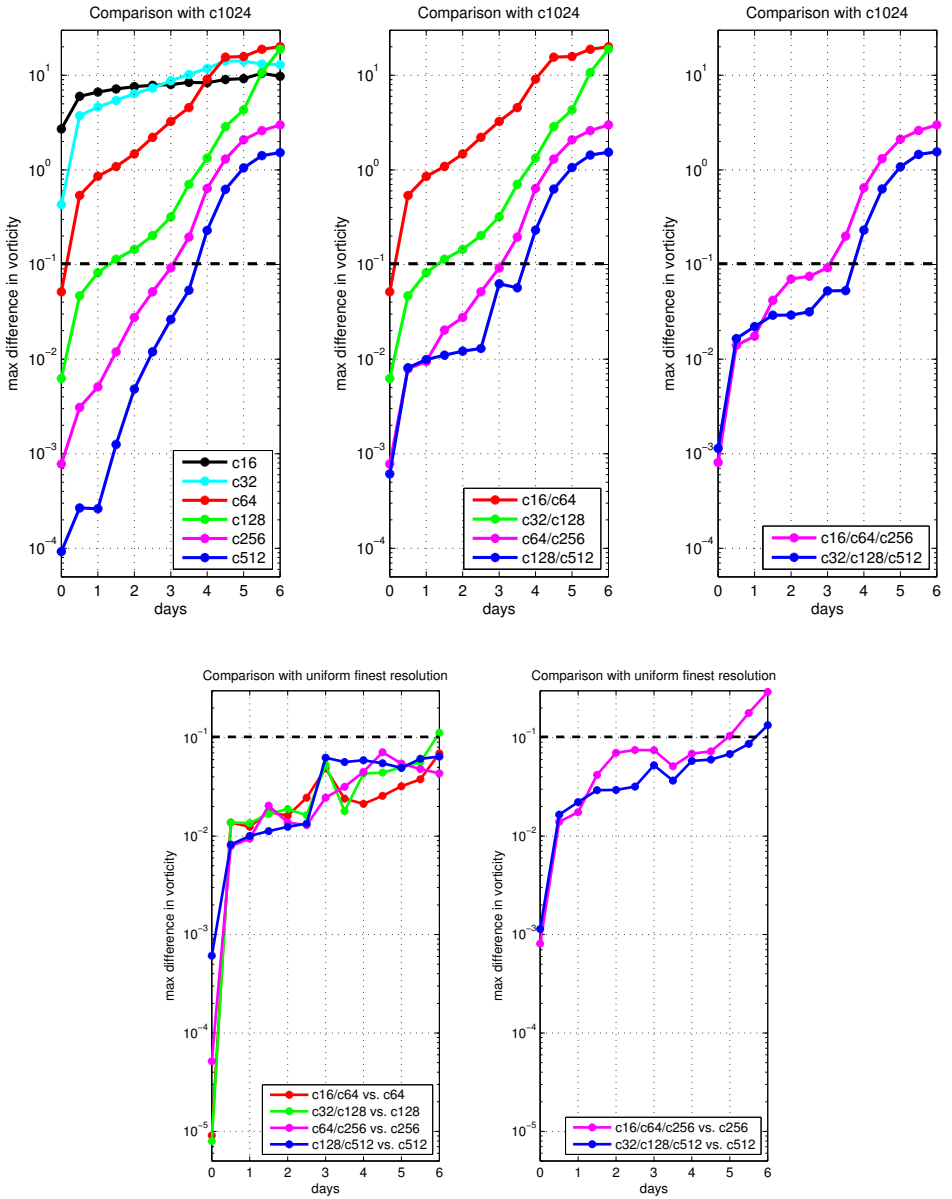

Figure 10. Plots of maximum differences in relative vorticity (in units of day^{-1}) between different runs of the barotropic-instability test of Section 5.3, shown at intervals of every half day. Plots for runs with the same *finest*-level resolution have the same color. Top: difference between uniform c1024 and (left to right) uniform, two-level, and three-level runs having resolution given in each legend. Bottom: difference between (left to right) two-level and three-level runs and the run with uniform resolution of the finest level in each case. On every plot, the refinement threshold of 0.102 day^{-1} from the coarsest level is marked with a dashed black line.

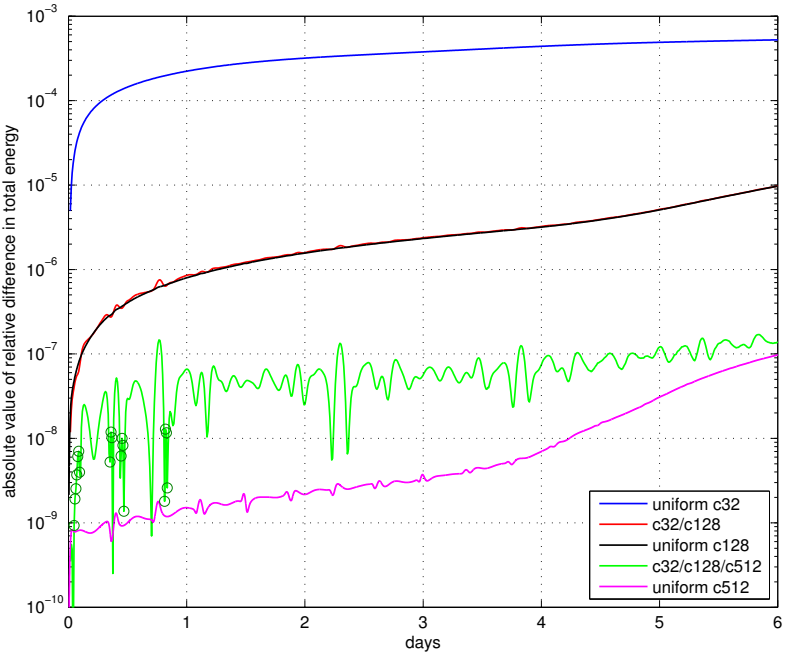

Figure 11. Plot of absolute value over time of the relative difference in total energy from initial value for five different runs of the barotropic-instability test of Section 5.3. Note that the curves for uniform c128 and for c32/c128 mostly overlap. The relative difference is *negative* at all steps after the initial time in all of these simulations with the exception of the c32/c128/c512 simulation, in which the relative difference is positive at the time steps marked with circles on the graph; as can be seen on the graph, all of these time steps occur before the end of day 1 and the relative difference never exceeds 2×10^{-8}.

loss, which suggests stability of the underlying numerical scheme. The three-level c32/c128/c512 simulation is the only one that shows total energy higher than its initial value at any stage of the simulation, but the stages where this occurs are all during the first day.

5.4. ***Gaussian pulse.*** The following example is included to test high-order convergence across refinement boundaries that are not characteristic. The initial velocity is zero, and the initial height field is a function of the latitude and is specified by a smoothed Gaussian with parameters $h_0 = 5000\,\mathrm{m}$ as background, $h_\delta = 500\,\mathrm{m}$ as maximum perturbation, and $w = \pi/10$ as angular width. With latitude ϕ, setting

$$\eta = \frac{\frac{1}{2}\pi - \phi}{w},$$

then

$$h(\eta) = \begin{cases} h_0 + h_\delta \exp(-4\eta^2)\cos^6(\frac{1}{2}\pi\eta) & \text{if } \eta < 1, \\ h_0 & \text{otherwise.} \end{cases} \tag{83}$$

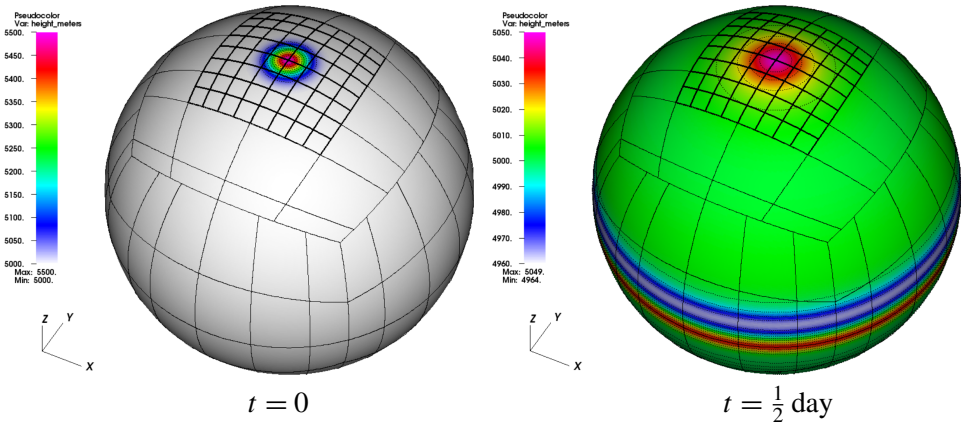

Figure 12. Total-height field for the Gaussian-pulse test case of Section 5.4 at (left) initial time $t = 0$ and (right) final time $t = \frac{1}{2}$ day. The base level is c128. There are fixed grids refined by a factor of 4 (hence a subset of c512) around the north pole, and these are shown with darker outlines than the coarse grids. Black contour lines (dotted) are drawn on each plot at values of the tick marks in the corresponding legend. Note the different color maps as initial h ranges from 5000 to 5500 meters and final h ranges from 4964 to 5049 meters.

The smoothing factor $\cos^6(\frac{1}{2}\pi\eta)$ is present in order to ensure that h is C^6. We calculate from times 0 to $\frac{1}{2}$ day, at which time the Gaussian has spread to the equator.

We pick time step $\Delta t = 0.4\,\text{day}/N_c$, and we find $c_{\max} = 6.30\,\text{rad/day}$, so the CFL number from (75) is 1.60. We run tests with uniform refinement, N_c a power of 2 and c32 up to c4096, and then with two levels, the coarser level having N_c a power of 2 and c32 up to c1024 and the finer level, with a refinement ratio of 4, consisting of grid cells encompassed by a square centered on the north pole, with side length half that of the north polar panel. Figure 12 shows h at initial time 0 and final time $\frac{1}{2}$ in a two-level c128/c512 run. The two-level runs are chosen so as to see the effect of a Gaussian initially contained within the finer level but then spreading past the coarse-fine boundary. Figure 13 shows a contour plot of calculated values of h in the two-level c128/512 run, at longitude 45°, as a function of latitude and time.

We take the solution with uniform c4096 to be a reference to compare results with the other resolutions. As seen in Table 3, the results approach fourth-order accuracy.

5.5. ***Zonal flow over an isolated mountain.*** Zonal flow over an isolated mountain is a key test of the performance of the model in the presence of topography. However, the traditionally employed shallow-water test of [61] has the disadvantage of being only C^0, hence preventing meaningful convergence studies beyond first order. Consequently, this paper uses a modified version of this test where the bottom

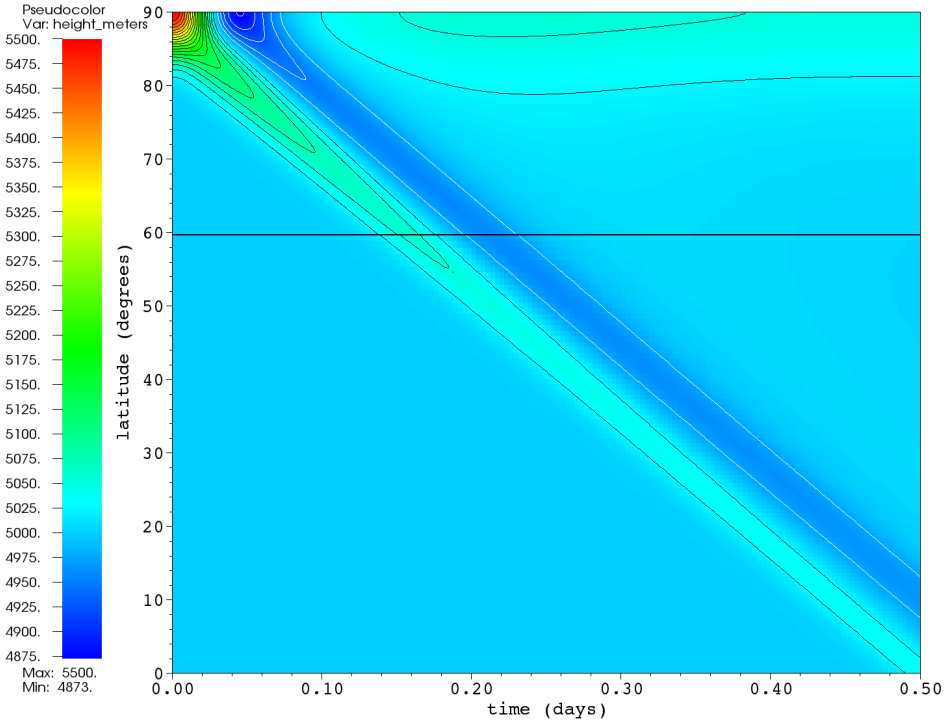

Figure 13. Total-height field for the Gaussian-pulse test case of Section 5.4 at longitude 45°, over all latitudes from initial time $t = 0$ to final time $t = \frac{1}{2}$ day. The base level is c128, and there is a finer level, a subset of c512, north of the refinement boundary indicated by the solid black line. At longitude 45°, this refinement boundary occurs at a corner of the grids shown in Figure 12. Contour lines are shown in black for every 25 meters above 5000 meters and in white for every 25 meters below 5000 meters.

topography is given by a C^3 cosine hill,

$$z_s = \frac{z_0}{4}\left[1 + \cos\left(\frac{\pi r}{R}\right)\right]^2, \tag{84}$$

where $R = \pi/9$ and $r^2 = \min\{R^2, (\lambda - \lambda_c)^2 + (\phi - \phi_c)^2\}$. The height of the mountain is $z_0 = 2000\,\mathrm{m}$, and its center is at $(\lambda_c, \phi_c) = (3\pi/2, \pi/6)$. The initial wind field is given by

$$u_\lambda = u_0 \cos\phi, \qquad u_\phi = 0 \tag{85}$$

and surface-height field by

$$H = h_0 - \frac{u_0}{2g}(u_0 + a\Omega)\sin^2\phi \tag{86}$$

with background height h_0 and velocity amplitude u_0 chosen to be

$$h_0 = 5960\,\mathrm{m}, \qquad u_0 = 20\,\mathrm{m}\cdot\mathrm{s}^{-1}. \tag{87}$$

Coarser resolution	Uniform resolution max error	rate	Two levels max error	rate
c32	1.489×10^{1}		1.286×10^{1}	
		1.20		1.12
c64	6.499×10^{0}		5.914×10^{0}	
		2.11		2.09
c128	1.509×10^{0}		1.390×10^{0}	
		2.90		2.86
c256	2.019×10^{-1}		1.912×10^{-1}	
		3.62		3.61
c512	1.641×10^{-2}		1.561×10^{-2}	
		3.95		3.95
c1024	1.059×10^{-3}		1.012×10^{-3}	

Table 3. Maximum difference between height in meters at final time with given resolutions and with uniform c4096 reference solution, and rates of convergence, for the Gaussian-pulse test case of Section 5.4. In the two-level runs, the refinement ratio between the coarser and finer levels is 4, so the resolution at the finer level is c128 through c4096.

We pick time step $\Delta t = 0.4\,\text{day}/N_c$, and we find $c_{\max} = 7.20\,\text{rad/day}$, so the CFL number from (75) is 1.83. We calculate up to 15 days with uniform refinement, N_c a power of 2 and c32 up to c1024.

Figure 14 shows the total height after 5, 10, and 15 days of the c128 solution. Although the mountain shape does not exactly match [61], we still observe an analogous appearance of a mix of large-scale Rossby waves and smaller-scale inertia-gravity waves.

We measure the error of the solution at a given time as the difference in total height between that solution and a c1024 reference solution. For runs with uniform resolutions from c32 to c512, Figure 15 shows the maximum magnitude of the error over the sphere after each day of the simulation. Note that up to day 6, the solution approaches fourth-order convergence. Figure 15 shows a jump in the maximum error in the c512 solution between day 6 and day 7 and a decrease in convergence rate to third order. In this case, the error in the c512 solution at day 7 is concentrated near one of the panel boundaries, in a region where the flow is tangent to the panel boundary. Where panel boundaries are characteristic, we expect a drop of one order of accuracy as is happening here in this case.

The longer-term solution approaches second-order convergence. This rate is expected because, as shown in [35; 47], once wave-breaking occurs the kinetic energy spectra of large-scale atmospheric flows will approach a decay rate of k^{-3}, corresponding to, at most, continuity of first derivatives of prognostic quantities.

Figure 16 shows the L^1 norm of the error after each day of the simulation, where the L^1 norm of a function is the integral of its absolute value over the sphere:

$$\|f\|_1 = \int |f|\, dA. \tag{88}$$

We see from Figure 16 that the L^1 norm of the error converges to fourth order with increasing refinement.

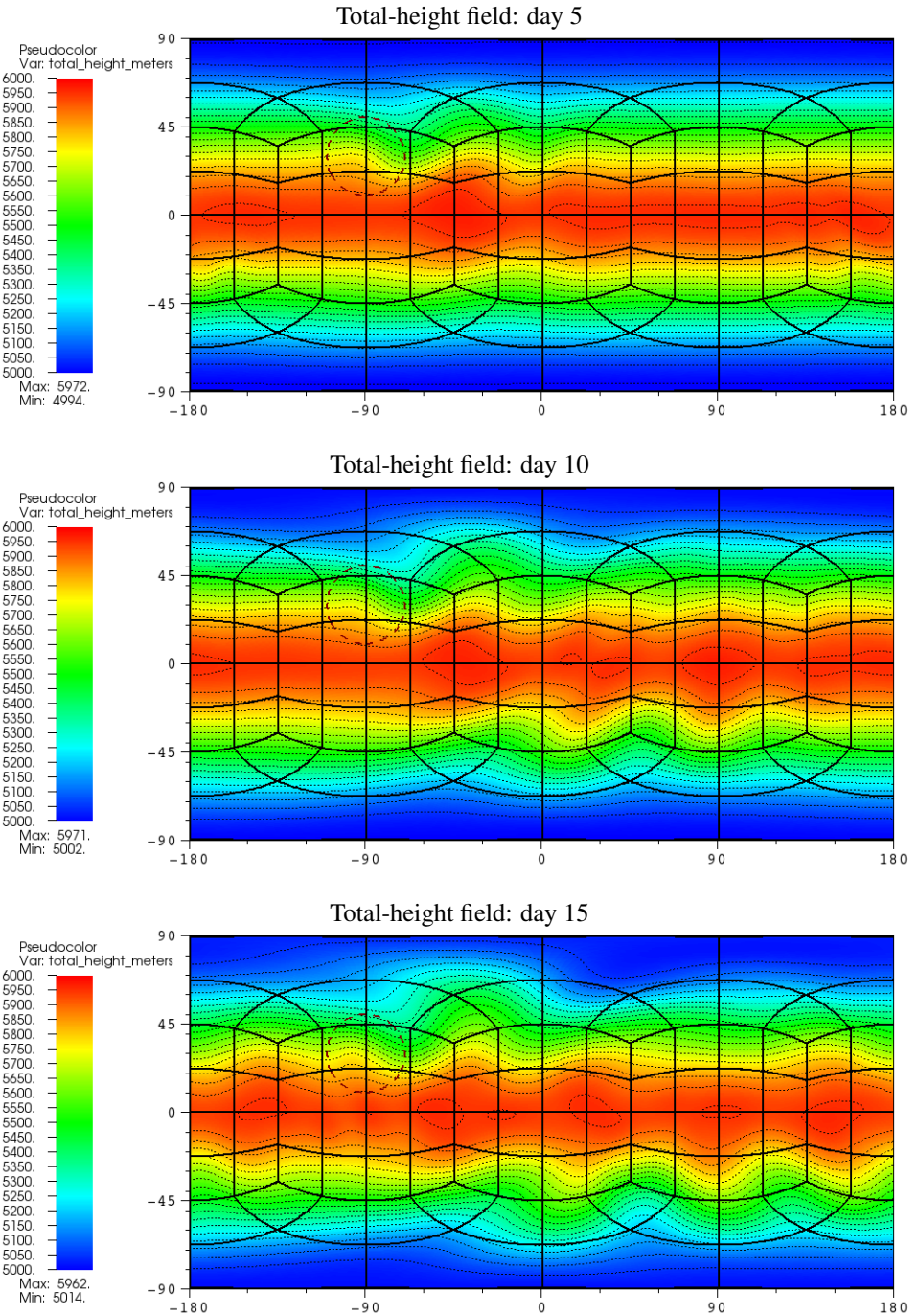

Figure 14. Total-height field for the C^3 mountain test case of Section 5.5, with c128 refinement. The base of the mountain is indicated with a dashed circle. Black contour lines (dotted) are drawn at intervals of 50 meters, at values of the tick marks in the legend.

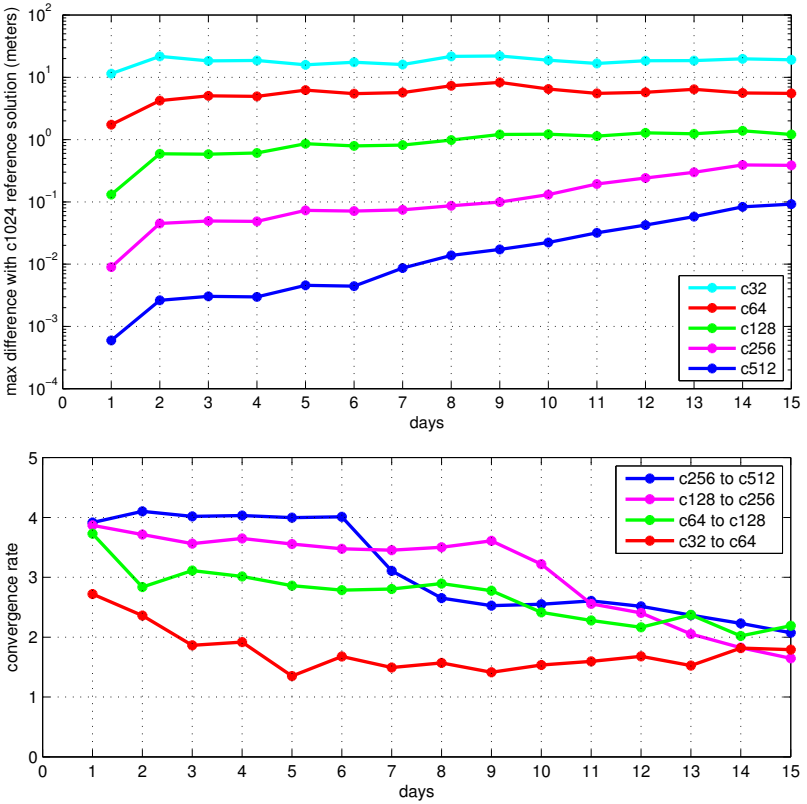

Figure 15. Top: plot of maximum differences over time between total height in meters in runs with given resolutions and the c1024 reference solution, for the C^3 mountain test case of Section 5.5. Bottom: plot of convergence rate over time, expressed as the base-2 logarithm of the ratio of the differences shown in the top plot for successive resolutions refined by a factor of 2.

6. Conclusions and future work

In this paper, we have presented a fourth-order-accurate finite-volume method on the cubed sphere. Despite formally third-order truncation-error accuracy at panel boundaries, the approach achieved fourth-order accuracy overall in smooth advection and the shallow-water equation test cases, with no evidence of panel-boundary artifacts. In addition, our results with adaptive mesh refinement show that, by using refined grids, it is possible to obtain overall solution error comparable to that on a uniform grid having the resolution of the finest level in the AMR hierarchy.

The next step is to extend this approach to the Euler equations on 3D thin spherical shells and complete a battery of dry atmospheric dynamical core tests. To that end, future work will include orography, which in 3D can be treated with several approaches such as cut-cell methods [59; 3], immersed-boundary methods [30], or

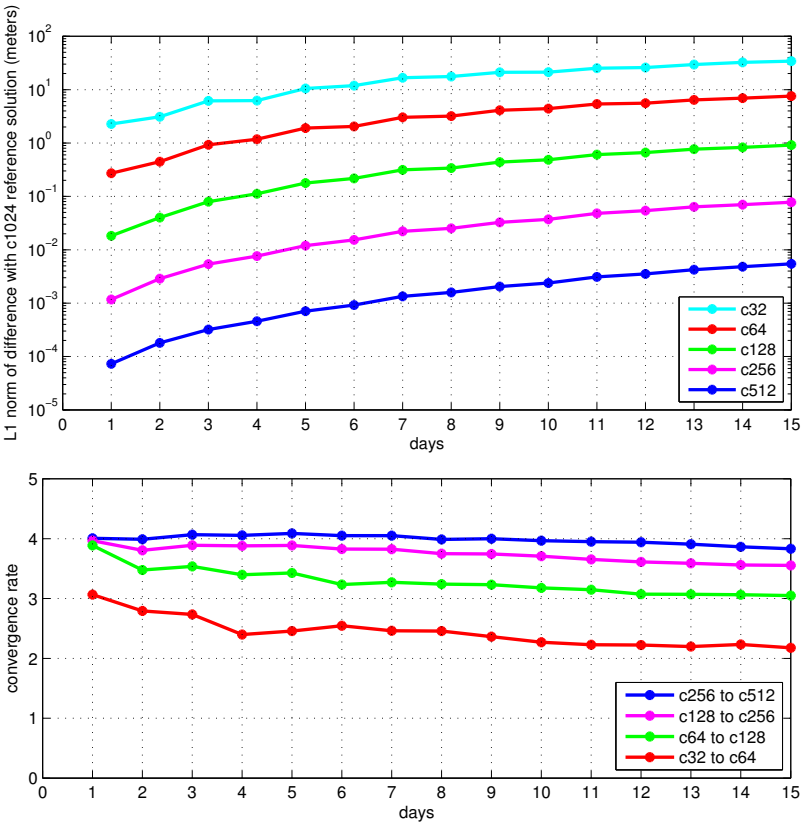

Figure 16. Top: plot of L^1 norm of differences over time between total height in meters in runs with given resolutions and the c1024 reference solution, for the C^3 mountain test case of Section 5.5. Bottom: plot of convergence rate over time, expressed as the base-2 logarithm of the ratio of the differences shown in the top plot for successive resolutions refined by a factor of 2.

terrain-following coordinates [14; 46]. In the near future, we anticipate incorporate climate cloud and radiation physics (such as that used in CESM [23]) with the goal of applying AMR to very high-resolution climate simulations.

Appendix A: Discrete undivided differences

This appendix gives the discrete undivided difference formulae that are used in Section 3 and their relationships to derivatives. The undivided differences are all denoted D with a subscript of α or β to indicate the direction in which the difference is taken and superscripts to indicate the order of the difference and whether the results are centered on the grid cells themselves (superscript c) or on their faces (superscript f).

A1. ***First differences on grid cells:*** $\boldsymbol{D^{1c\{C,L,R\}}_{\{\alpha,\beta\}}}$**.** First differences D^{1cC}_{α} and D^{1cC}_{β} on a grid cell take the 3-point centered finite-difference stencils:

$$(D^{1cC}_{\alpha}a)_{i,j} = \frac{a_{i+1,j} - a_{i-1,j}}{2}, \qquad (D^{1cC}_{\beta}a)_{i,j} = \frac{a_{i,j+1} - a_{i,j-1}}{2}. \tag{A-1}$$

One-sided differences $D^{1c\{L,R\}}_{\alpha}$ are given by

$$(D^{1cL}_{\alpha}a)_{i,j} = \frac{-3a_{i,j} + 4a_{i+1,j} - a_{i+2,j}}{2}, \tag{A-2}$$

$$(D^{1cR}_{\alpha}a)_{i,j} = \frac{a_{i-2,j} - 4a_{i-1,j} + 3a_{i,j}}{2} \tag{A-3}$$

and one-sided differences $D^{1c\{L,R\}}_{\beta}$ by

$$(D^{1cL}_{\beta}a)_{i,j} = \frac{-3a_{i,j} + 4a_{i,j+1} - a_{i,j+2}}{2}, \tag{A-4}$$

$$(D^{1cR}_{\beta}a)_{i,j} = \frac{a_{i,j-2} - 4a_{i,j-1} + 3a_{i,j}}{2}. \tag{A-5}$$

These differences are related to partial derivatives as

$$D^{1c\{C,L,R\}}_{\alpha}a = \Delta\alpha\frac{\partial a}{\partial\alpha} + O((\Delta\alpha)^3), \qquad D^{1c\{C,L,R\}}_{\beta}a = \Delta\beta\frac{\partial a}{\partial\beta} + O((\Delta\beta)^3). \tag{A-6}$$

A2. ***Second differences on grid cells:*** $\boldsymbol{D^{2c}_{\{\alpha,\beta\}}}$**.** Second differences D^{2c}_{α} and D^{2c}_{β} take the 3-point centered finite-difference stencils:

$$(D^{2c}_{\alpha}a)_{i,j} = a_{i+1,j} - 2a_{i,j} + a_{i-1,j}, \qquad (D^{2c}_{\beta}a)_{i,j} = a_{i,j+1} - 2a_{i,j} + a_{i,j-1}. \tag{A-7}$$

These differences are related to partial derivatives as

$$D^{2c}_{\alpha}a = (\Delta\alpha)^2\frac{\partial^2 a}{\partial\alpha^2} + O((\Delta\alpha)^4), \qquad D^{2c}_{\beta}a = (\Delta\beta)^2\frac{\partial^2 a}{\partial\beta^2} + O((\Delta\beta)^4). \tag{A-8}$$

A3. ***First transverse differences on faces of grid cells:*** $\boldsymbol{D^{1f}_{\{\alpha,\beta\}}}$**.** The first transverse differences, D^{1f}_{β} on faces of constant α and D^{1f}_{α} on faces of constant β, take the 3-point centered finite-difference stencils:

$$(D^{1f}_{\beta}a)_{i+\frac{1}{2},j} = \frac{a_{i+\frac{1}{2},j+1} - a_{i+\frac{1}{2},j-1}}{2}, \tag{A-9}$$

$$(D^{1f}_{\alpha}a)_{i,j+\frac{1}{2}} = \frac{a_{i+1,j+\frac{1}{2}} - a_{i-1,j+\frac{1}{2}}}{2}. \tag{A-10}$$

These differences are related to partial derivatives as

$$D^{1f}_{\beta}a = \Delta\beta\frac{\partial a}{\partial\beta} + O((\Delta\beta)^3), \qquad D^{1f}_{\alpha}a = \Delta\alpha\frac{\partial a}{\partial\alpha} + O((\Delta\alpha)^3). \tag{A-11}$$

A4. ***Second transverse differences on faces of grid cells:*** $\boldsymbol{D^{2\mathrm{f}}_{\{\alpha,\beta\}}}$**.** The second transverse differences, $D^{2\mathrm{f}}_{\beta}$ on faces of constant α and $D^{2\mathrm{f}}_{\alpha}$ on faces of constant β, take the 3-point centered finite-difference stencils:

$$(D^{2\mathrm{f}}_{\beta}a)_{i+\frac{1}{2},j} = a_{i+\frac{1}{2},j-1} - 2a_{i+\frac{1}{2},j} + a_{i+\frac{1}{2},j+1}, \tag{A-12}$$

$$(D^{2\mathrm{f}}_{\alpha}a)_{i,j+\frac{1}{2}} = a_{i-1,j+\frac{1}{2}} - 2a_{i,j+\frac{1}{2}} + a_{i+1,j+\frac{1}{2}}. \tag{A-13}$$

These differences are related to partial derivatives as

$$D^{2\mathrm{f}}_{\beta}a = (\Delta\beta)^2\frac{\partial^2 a}{\partial\beta^2} + O((\Delta\beta)^4), \qquad D^{2\mathrm{f}}_{\alpha}a = (\Delta\alpha)^2\frac{\partial^2 a}{\partial\alpha^2} + O((\Delta\alpha)^4). \tag{A-14}$$

A5. ***Fifth differences on faces of grid cells:*** $\boldsymbol{D^{5\mathrm{f}}_{\{\alpha,\beta\}}}$**.** For the artificial dissipation in Step (9) in Section 3.4, we need fifth undivided differences on faces, from data on grid cells:

$$(D^{5\mathrm{f}}_{\alpha}a)_{i+\frac{1}{2},j} = 10(a_{i+1,j} - a_{i,j}) - 5(a_{i+2,j} - a_{i-1,j}) + a_{i+3,j} - a_{i-2,j}, \tag{A-15}$$

$$(D^{5\mathrm{f}}_{\beta}a)_{i,j+\frac{1}{2}} = 10(a_{i,j+1} - a_{i,j}) - 5(a_{i,j+2} - a_{i,j-1}) + a_{i,j+3} - a_{i,j-2}. \tag{A-16}$$

These differences are related to partial derivatives as

$$D^{5\mathrm{f}}_{\alpha}a = (\Delta\alpha)^5\frac{\partial^5 a}{\partial\alpha^5} + O((\Delta\alpha)^7), \qquad D^{5\mathrm{f}}_{\beta}a = (\Delta\beta)^5\frac{\partial^5 a}{\partial\beta^5} + O((\Delta\beta)^7). \tag{A-17}$$

Appendix B: High-order averages over grid cells and faces

We use angle brackets $\langle\cdot\rangle_{i,j}$ to denote the average of a quantity over a computational grid cell $V_{i,j}$. An average over the face of $V_{i,j}$ where $\alpha = \alpha_i \pm \frac{1}{2}\Delta\alpha$ and $\beta \in [\beta_j - \frac{1}{2}\Delta\beta, \beta_j + \frac{1}{2}\Delta\beta]$ is denoted by $\langle\cdot\rangle_{i\pm\frac{1}{2},j}$, and an average over the face where $\beta = \beta_j \pm \frac{1}{2}\Delta\beta$ and $\alpha \in [\alpha_i - \frac{1}{2}\Delta\alpha, \alpha_i + \frac{1}{2}\Delta\alpha]$ is denoted by $\langle\cdot\rangle_{i,j\pm\frac{1}{2}}$.

B1. ***Exact*** $\boldsymbol{\langle J\rangle}$ ***on grid cells.*** For J defined in (5), the average $\langle J\rangle$ on a grid cell $V_{i,j}$ can be computed exactly:

$$\begin{aligned}\langle J\rangle_{i,j} &= \frac{1}{\Delta\alpha\,\Delta\beta}\int_{\beta_j-\frac{1}{2}\Delta\beta}^{\beta_j+\frac{1}{2}\Delta\beta}\int_{\alpha_i-\frac{1}{2}\Delta\alpha}^{\alpha_i+\frac{1}{2}\Delta\alpha} J\,d\alpha\,d\beta \\ &= \frac{r^2}{\Delta\alpha\,\Delta\beta}\sum_{p=0}^{1}\sum_{q=0}^{1}(-1)^{p+q}\tan^{-1}\frac{X_pY_q}{\sqrt{1+X_p^2+Y_q^2}},\end{aligned} \tag{B-18}$$

where $X_0 = \tan(\alpha_i - \frac{1}{2}\Delta\alpha)$, $X_1 = \tan(\alpha_i + \frac{1}{2}\Delta\alpha)$, $Y_0 = \tan(\beta_j - \frac{1}{2}\Delta\beta)$, and $Y_1 = \tan(\beta_j + \frac{1}{2}\Delta\beta)$.

B2. ***Exact $\langle J \rangle$ on faces of grid cells.*** We can also compute exactly the average of J over faces of grid cells.

- On faces of constant $\alpha = \alpha_i + \frac{1}{2}\Delta\alpha$, with β extending from $\beta_j - \frac{1}{2}\Delta\beta$ to $\beta_j + \frac{1}{2}\Delta\beta$:

$$\langle J \rangle_{i+\frac{1}{2},j} = \int_{\beta_j - \frac{1}{2}\Delta\beta}^{\beta_j + \frac{1}{2}\Delta\beta} J \, d\beta = \frac{r^2 Y_1}{\sqrt{1 + X^2 + Y_1^2}} - \frac{r^2 Y_0}{\sqrt{1 + X^2 + Y_0^2}}, \tag{B-19}$$

  where $X = \tan(\alpha)$, $Y_0 = \tan(\beta_j - \frac{1}{2}\Delta\beta)$, and $Y_1 = \tan(\beta_j + \frac{1}{2}\Delta\beta)$.

- On faces of constant $\beta = \beta_j + \frac{1}{2}\Delta\beta$, with α extending from $\alpha_i - \frac{1}{2}\Delta\alpha$ to $\alpha_i + \frac{1}{2}\Delta\alpha$:

$$\langle J \rangle_{i,j+\frac{1}{2}} = \int_{\alpha_i - \frac{1}{2}\Delta\alpha}^{\alpha_i + \frac{1}{2}\Delta\alpha} J \, d\alpha = \frac{r^2 X_1}{\sqrt{1 + X_1^2 + Y^2}} - \frac{r^2 X_0}{\sqrt{1 + X_0^2 + Y^2}}, \tag{B-20}$$

  where $X_0 = \tan(\alpha_i - \frac{1}{2}\Delta\alpha)$, $X_1 = \tan(\alpha_i + \frac{1}{2}\Delta\alpha)$, and $Y = \tan(\beta)$.

B3. ***High-order conversion between averaged and centered values.***

- If we have a at centers of grid cells, then by expanding Taylor series, we can obtain averages of a over grid cells:

$$\langle a \rangle_{i,j} = a_{i,j} + \frac{(\Delta\alpha)^2}{24}\left(\frac{\partial^2 a}{\partial\alpha^2}\right)_{i,j} + \frac{(\Delta\beta)^2}{24}\left(\frac{\partial^2 a}{\partial\beta^2}\right)_{i,j} + O((\Delta\alpha)^4, (\Delta\alpha)^2(\Delta\beta)^2, (\Delta\beta)^4). \tag{B-21}$$

  Using the discrete-differences notation of Appendix A2, this can be written as

$$\langle a \rangle_{i,j} = a_{i,j} + \tfrac{1}{24}(D_\alpha^{2c} a)_{i,j} + \tfrac{1}{24}(D_\beta^{2c} a)_{i,j} + O((\Delta\alpha)^4, (\Delta\alpha)^2(\Delta\beta)^2, (\Delta\beta)^4), \tag{B-22}$$

$$a_{i,j} = \langle a \rangle_{i,j} - \tfrac{1}{24}(D_\alpha^{2c} \langle a \rangle)_{i,j} - \tfrac{1}{24}(D_\beta^{2c} \langle a \rangle)_{i,j} + O((\Delta\alpha)^4, (\Delta\alpha)^2(\Delta\beta)^2, (\Delta\beta)^4). \tag{B-23}$$

- With a at centers of faces of grid cells, we can also expand the Taylor series to obtain an approximation to averages over faces:

$$\langle a \rangle_{i+\frac{1}{2},j} = a_{i+\frac{1}{2},j} + \frac{(\Delta\beta)^2}{24}\left(\frac{\partial^2 a}{\partial\beta^2}\right)_{i+\frac{1}{2},j} + O((\Delta\beta)^4), \tag{B-24}$$

$$\langle a \rangle_{i,j+\frac{1}{2}} = a_{i,j+\frac{1}{2}} + \frac{(\Delta\alpha)^2}{24}\left(\frac{\partial^2 a}{\partial\alpha^2}\right)_{i,j+\frac{1}{2}} + O((\Delta\alpha)^4). \tag{B-25}$$

Hence, taking the discrete differences of Appendix A4,

$$\langle a\rangle_{i+\frac{1}{2},j} = a_{i+\frac{1}{2},j} + \tfrac{1}{24}(D_\beta^{2\mathrm{f}} a)_{i+\frac{1}{2},j} + O((\Delta\beta)^4), \tag{B-26}$$

$$a_{i+\frac{1}{2},j} = \langle a\rangle_{i+\frac{1}{2},j} - \tfrac{1}{24}(D_\beta^{2\mathrm{f}} \langle a\rangle)_{i+\frac{1}{2},j} + O((\Delta\beta)^4), \tag{B-27}$$

$$\langle a\rangle_{i,j+\frac{1}{2}} = a_{i,j+\frac{1}{2}} + \tfrac{1}{24}(D_\alpha^{2\mathrm{f}} a)_{i,j+\frac{1}{2}} + O((\Delta\alpha)^4), \tag{B-28}$$

$$a_{i,j+\frac{1}{2}} = \langle a\rangle_{i,j+\frac{1}{2}} - \tfrac{1}{24}(D_\alpha^{2\mathrm{f}} \langle a\rangle)_{i,j+\frac{1}{2}} + O((\Delta\alpha)^4). \tag{B-29}$$

B4. ***High-order product formulae.***

- As shown in [10], the average of a product of a and b over a grid cell is

$$\langle ab\rangle = \langle a\rangle\langle b\rangle + \frac{(\Delta\alpha)^2}{12}\frac{\partial a}{\partial\alpha}\frac{\partial b}{\partial\alpha} + \frac{(\Delta\beta)^2}{12}\frac{\partial a}{\partial\beta}\frac{\partial b}{\partial\beta} + O((\Delta\alpha)^4, (\Delta\alpha)^2(\Delta\beta)^2, (\Delta\beta)^4). \tag{B-30}$$

Hence on $V_{i,j}$, using (A-6) with the undivided differences $D_\alpha^{1\mathrm{cC}}$ and $D_\beta^{1\mathrm{cC}}$ from Appendix A1,

$$\langle ab\rangle_{i,j} = \langle a\rangle_{i,j}\langle b\rangle_{i,j} + \tfrac{1}{12}(D_\alpha^{1\mathrm{cC}} a)_{i,j}(D_\alpha^{1\mathrm{cC}} b)_{i,j} + \tfrac{1}{12}(D_\beta^{1\mathrm{cC}} a)_{i,j}(D_\beta^{1\mathrm{cC}} b)_{i,j} + O((\Delta\alpha)^4, (\Delta\alpha)^2(\Delta\beta)^2, (\Delta\beta)^4), \tag{B-31}$$

and the average of one of the factors can be obtained from the average of the product by

$$\langle b\rangle_{i,j} = \frac{\langle ab\rangle_{i,j} - \tfrac{1}{12}\left(D_\alpha^{1\mathrm{cC}}\frac{\langle ab\rangle}{\langle a\rangle}\right)_{i,j}(D_\alpha^{1\mathrm{cC}}\langle a\rangle)_{i,j} - \tfrac{1}{12}\left(D_\beta^{1\mathrm{cC}}\frac{\langle ab\rangle}{\langle a\rangle}\right)_{i,j}(D_\beta^{1\mathrm{cC}}\langle a\rangle)_{i,j}}{\langle a\rangle_{i,j}} + O((\Delta\alpha)^4, (\Delta\alpha)^2(\Delta\beta)^2, (\Delta\beta)^4). \tag{B-32}$$

In (B-32), we can substitute the one-sided $D_\alpha^{1\mathrm{cL}}$ or $D_\alpha^{1\mathrm{cR}}$ for the centered $D_\alpha^{1\mathrm{cC}}$ if $V_{i-1,j}$ or $V_{i+1,j}$, respectively, is not a grid cell of the panel containing $V_{i,j}$. Similarly, we can substitute $D_\beta^{1\mathrm{cL}}$ or $D_\beta^{1\mathrm{cR}}$ for $D_\beta^{1\mathrm{cC}}$ if $V_{i,j-1}$ or $V_{i,j+1}$, respectively, is not a grid cell of the panel containing $V_{i,j}$.

- Also from [10] and using (A-11), the average of a product of a and b over the face of a grid cell with constant α is

$$\langle ab\rangle_{i+\frac{1}{2},j} = \langle a\rangle_{i+\frac{1}{2},j}\langle b\rangle_{i+\frac{1}{2},j} + \tfrac{1}{12}(D_\beta^{1\mathrm{f}} a)_{i+\frac{1}{2},j}(D_\beta^{1\mathrm{f}} b)_{i+\frac{1}{2},j} + O((\Delta\beta)^4) \tag{B-33}$$

and over the face of a grid cell with constant β is

$$\langle ab\rangle_{i,j+\frac{1}{2}} = \langle a\rangle_{i,j+\frac{1}{2}}\langle b\rangle_{i,j+\frac{1}{2}} + \tfrac{1}{12}(D_\alpha^{1\mathrm{f}} a)_{i,j+\frac{1}{2}}(D_\alpha^{1\mathrm{f}} b)_{i,j+\frac{1}{2}} + O((\Delta\alpha)^4). \tag{B-34}$$

References

[1] M. Adams, P. Colella, D. T. Graves, J. N. Johnson, H. S. Johansen, N. D. Keen, T. J. Ligocki, D. F. Martin, P. W. McCorquodale, D. Modiano, P. O. Schwartz, T. D. Sternberg, and B. Van Straalen, *Chombo software package for AMR applications: design document*, Tech. Report LBNL-6616E, Lawrence Berkeley National Laboratory, 2014.

[2] L. Bao, R. D. Nair, and H. M. Tufo, *A mass and momentum flux-form high-order discontinuous Galerkin shallow water model on the cubed-sphere*, J. Comput. Phys. **271** (2014), 224–243. MR 3209599

[3] M. F. Barad, P. Colella, and S. G. Schladow, *An adaptive cut-cell method for environmental fluid mechanics*, Internat. J. Numer. Methods Fluids **60** (2009), no. 5, 473–514. MR 2010d:76022

[4] J. R. Bates, F. H. M. Semazzi, R. W. Higgins, and S. R. M. Barros, *Integration of the shallow water equations on the sphere using a vector semi-Lagrangian scheme with a multigrid solver*, Mon. Weather Rev. **118** (1990), no. 8, 1615–1627.

[5] S. Blaise and A. St-Cyr, *A dynamic hp-adaptive discontinuous Galerkin method for shallow-water flows on the sphere with application to a global tsunami simulation*, Mon. Weather Rev. **140** (2012), no. 3, 978–996.

[6] C. Chaplin and P. Colella, *A single stage flux-corrected transport algorithm for high-order finite-volume methods*, Tech. report, 2015, Submitted to Commun. Appl. Math. Comput. Sci. arXiv 1506.02999v1

[7] C. Chen, X. Li, X. Shen, and F. Xiao, *Global shallow water models based on multi-moment constrained finite volume method and three quasi-uniform spherical grids*, J. Comput. Phys. **271** (2014), 191–223. MR 3209598

[8] C. Chen and F. Xiao, *Shallow water model on cubed-sphere by multi-moment finite volume method*, J. Comput. Phys. **227** (2008), no. 10, 5019–5044. MR 2009e:86001

[9] C. Chen, F. Xiao, and X. Li, *An adaptive multimoment global model on a cubed sphere*, Mon. Weather Rev. **139** (2011), no. 2, 523–548.

[10] P. Colella, M. R. Dorr, J. A. F. Hittinger, and D. F. Martin, *High-order, finite-volume methods in mapped coordinates*, J. Comput. Phys. **230** (2011), no. 8, 2952–2976. MR 2012d:65245 Zbl 1218.65119

[11] R. Comblen, S. Legrand, E. Deleersnijder, and V. Legat, *A finite element method for solving the shallow water equations on the sphere*, Ocean Model. **38** (2009), no. 1–3, 12–23.

[12] J. Côté and A. Staniforth, *An accurate and efficient finite-element global model of the shallow-water equations*, Mon. Weather Rev. **118** (1990), no. 12, 2707–2717.

[13] J. M. Dennis, J. Edwards, K. J. Evans, O. Guba, P. H. Lauritzen, A. A. Mirin, A. St-Cyr, M. A. Taylor, and P. H. Worley, *CAM-SE: a scalable spectral element dynamical core for the Community Atmosphere Model*, Int. J. High Perform. C. **26** (2012), no. 1, 74–89.

[14] T. Gal-Chen and R. C. J. Somerville, *On the use of a coordinate transformation for the solution of the Navier–Stokes equations*, J. Computational Phys. **17** (1975), 209–228. MR 51 #2470 Zbl 0297.76020

[15] J. Galewsky, R. K. Scott, and L. M. Polvani, *An initial-value problem for testing numerical models of the global shallow-water equations*, Tellus A **56** (2004), no. 5, 429–440.

[16] A. Gassmann, *A global hexagonal C-grid non-hydrostatic dynamical core (ICON-IAP) designed for energetic consistency*, Q. J. Roy. Meteor. Soc. **139** (2013), no. 670, 152–175.

[17] F. X. Giraldo, J. S. Hesthaven, and T. Warburton, *Nodal high-order discontinuous Galerkin methods for the spherical shallow water equations*, J. Comput. Phys. **181** (2002), no. 2, 499–525. MR 2003g:86004 Zbl 1178.76268

[18] M. Govett, J. Middlecoff, and T. Henderson, *Running the NIM next-generation weather model on GPUs*, 10th IEEE/ACM international conference on cluster, cloud and grid computing (Melbourne, 2010) (M. Parashar and R. Buyya, eds.), IEEE Computer Society, Los Lamitos, CA, 2010, pp. 792–796.

[19] S. M. Guzik, P. McCorquodale, and P. Colella, *A freestream-preserving high-order finite-volume method for mapped grids with adaptive-mesh refinement*, 50th AIAA aerospace sciences meeting (Nashville, TN, 2012), AIAA, Reston, VA, 2012, p. 0574.

[20] E. Hairer, S. P. Nørsett, and G. Wanner, *Solving ordinary differential equations, I: Nonstiff problems*, 2nd ed., Springer Series in Computational Mathematics, no. 8, Springer, Berlin, 1993. MR 94c:65005

[21] R. Heikes and D. A. Randall, *Numerical integration of the shallow-water equations on a twisted icosahedral grid, I: Basic design and results of tests*, Mon. Weather Rev. **123** (1995), no. 6, 1862–1880.

[22] J. Hilditch and P. Colella, *A projection method for low Mach number fast chemistry reacting flow*, 35th AIAA aerospace sciences meeting (Reno, NV, 1997), AIAA, Reston, VA, 1997, p. 0263.

[23] J. W. Hurrell, M. M. Holland, P. R. Gent, S. Ghan, J. E. Kay, P. J. Kushner, J.-F. Lamarque, W. G. Large, D. Lawrence, K. Lindsay, W. H. Lipscomb, M. C. Long, N. Mahowald, D. R. Marsh, R. B. Neale, P. Rasch, S. Vavrus, M. Vertenstein, D. Bader, W. D. Collins, J. J. Hack, J. Kiehl, and S. Marshall, *The community earth system model: a framework for collaborative research*, B. Am. Meteorol. Soc. **94** (2013), no. 9, 1339–1360.

[24] S. Ii and F. Xiao, *A global shallow water model using high order multi-moment constrained finite volume method and icosahedral grid*, J. Comput. Phys. **229** (2010), no. 5, 1774–1796. MR 2010i:65179

[25] R. Jakob-Chien, J. J. Hack, and D. L. Williamson, *Spectral transform solutions to the shallow water test set*, J. Comput. Phys. **119** (1995), no. 1, 164–187. Zbl 0878.76059

[26] M. Läuter, F. X. Giraldo, D. Handorf, and K. Dethloff, *A discontinuous Galerkin method for the shallow water equations in spherical triangular coordinates*, J. Comput. Phys. **227** (2008), no. 24, 10226–10242. MR 2467951 Zbl 1218.76028

[27] X. Li, D. Chen, X. Peng, K. Takahashi, and F. Xiao, *A multimoment finite-volume shallow-water model on the Yin–Yang overset spherical grid*, Mon. Weather Rev. **136** (2008), no. 8, 3066–3086.

[28] S.-J. Lin, *A "vertically Lagrangian" finite-volume dynamical core for global models*, Mon. Weather Rev. **132** (2004), no. 10, 2293–2307.

[29] S.-J. Lin and R. B. Rood, *An explicit flux-form semi-Lagrangian shallow-water model on the sphere*, Q. J. Roy. Meteor. Soc. **123** (1997), no. 544, 2477–2498.

[30] K. A. Lundquist, F. K. Chow, and J. K. Lundquist, *An immersed boundary method for the weather research and forecasting model*, Mon. Weather Rev. **138** (2010), no. 3, 796–817.

[31] P. McCorquodale, M. R. Dorr, J. A. F. Hittinger, and P. Colella, *High-order finite-volume methods for hyperbolic conservation laws on mapped multiblock grids*, J. Comput. Phys. **288** (2015), 181–195. MR 3320206

[32] P. McCorquodale and P. Colella, *A high-order finite-volume method for conservation laws on locally refined grids*, Commun. Appl. Math. Comput. Sci. **6** (2011), no. 1, 1–25. MR 2012h:65181 Zbl 1252.65163

[33] R. D. Nair, S. J. Thomas, and R. D. Loft, *A discontinuous Galerkin transport scheme on the cubed sphere*, Mon. Weather Rev. **133** (2005), no. 4, 814–828.

[34] R. D. Nair and P. H. Lauritzen, *A class of deformational flow test cases for linear transport problems on the sphere*, J. Comput. Phys. **229** (2010), no. 23, 8868–8887. MR 2011f:86010 Zbl 1282.86012

[35] G. D. Nastrom and K. S. Gage, *A climatology of atmospheric wavenumber spectra of wind and temperature observed by commercial aircraft*, J. Atmos. Sci. **42** (1985), no. 9, 950–960.

[36] W. M. Putman and S.-J. Lin, *A finite-volume dynamical core on the cubed-sphere grid*, Numerical modeling of space plasma flows: ASTRONUM 2008 (Saint John, United States Virgin Islands, 2008) (N. V. Pogorelov, E. Audit, P. Colella, and G. P. Zank, eds.), ASP Conference Series, no. 406, Astronomical Society of the Pacific, San Francisco, 2009, pp. 268–276.

[37] W. M. Putman and S.-J. Lin, *Finite-volume transport on various cubed-sphere grids*, J. Comput. Phys. **227** (2007), no. 1, 55–78. MR 2008j:86001 Zbl 1126.76038

[38] A. Qaddouri, J. Pudykiewicz, M. Tanguay, C. Girard, and J. Côté, *Experiments with different discretizations for the shallow-water equations on a sphere*, Q. J. Roy. Meteor. Soc. **138** (2012), no. 665, 989–1003.

[39] T. Ringler, L. Ju, and M. Gunzburger, *A multiresolution method for climate system modeling: application of spherical centroidal Voronoi tessellations*, Ocean Dynam. **58** (2008), no. 5–6, 475–498.

[40] T. D. Ringler, D. Jacobsen, M. Gunzburger, L. Ju, M. Duda, and W. Skamarock, *Exploring a multiresolution modeling approach within the shallow-water equations*, Mon. Weather Rev. **139** (2011), no. 11, 3348–3368.

[41] H. Ritchie, *Application of the semi-Lagrangian method to a spectral model of the shallow water equations*, Mon. Weather Rev. **116** (1988), no. 8, 1587–1598.

[42] C. Ronchi, R. Iacono, and P. S. Paolucci, *The "cubed sphere": a new method for the solution of partial differential equations in spherical geometry*, J. Comput. Phys. **124** (1996), no. 1, 93–114. MR 96k:86001

[43] J. A. Rossmanith, *A wave propagation method for hyperbolic systems on the sphere*, J. Comput. Phys. **213** (2006), no. 2, 629–658. MR 2007i:65065 Zbl 1089.65088

[44] R. Sadourny, *Conservative finite-difference approximations of the primitive equations on quasi-uniform spherical grids*, Mon. Weather Rev. **100** (1972), no. 2, 136–144.

[45] M. Satoh, T. Matsuno, H. Tomita, H. Miura, T. Nasuno, and S. Iga, *Nonhydrostatic icosahedral atmospheric model (NICAM) for global cloud resolving simulations*, J. Comput. Phys. **227** (2008), no. 7, 3486–3514. MR 2009b:86006 Zbl 1132.86311

[46] C. Schär, D. Leuenberger, O. Fuhrer, D. Lüthi, and C. Girard, *A new terrain-following vertical coordinate formulation for atmospheric prediction models*, Mon. Weather Rev. **130** (2002), no. 10, 2459–2480.

[47] W. C. Skamarock, *Evaluating mesoscale NWP models using kinetic energy spectra*, Mon. Weather Rev. **132** (2004), no. 12, 3019–3032.

[48] W. C. Skamarock, J. B. Klemp, M. G. Duda, L. D. Fowler, S.-H. Park, and T. D. Ringler, *A multiscale nonhydrostatic atmospheric model using centroidal Voronoi tesselations and C-grid staggering*, Mon. Weather Rev. **140** (2012), no. 9, 3090–3105.

[49] A. St-Cyr, C. Jablonowski, J. M. Dennis, H. M. Tufo, and S. J. Thomas, *A comparison of two shallow-water models with nonconforming adaptive grids*, Mon. Weather Rev. **136** (2008), no. 6, 1898–1922.

[50] A. Staniforth and J. Thuburn, *Horizontal grids for global weather and climate prediction models: a review*, Q. J. Roy. Meteor. Soc. **138** (2012), no. 662, 1–26.

[51] M. Taylor, J. Tribbia, and M. Iskandarani, *The spectral element method for the shallow water equations on the sphere*, J. Comput. Phys. **130** (1997), no. 1, 92–108. Zbl 0868.76072

[52] S. J. Thomas and R. D. Loft, *The NCAR spectral element climate dynamical core: semi-implicit Eulerian formulation*, J. Sci. Comput. **25** (2005), no. 1-2, 307–322. MR 2007b:86019 Zbl 1203.86013

[53] M. A. Tolstykh, *Vorticity-divergence semi-Lagrangian shallow-water model of the sphere based on compact finite differences*, J. Comput. Phys. **179** (2002), no. 1, 180–200. MR 2003e:76085a Zbl 1060.76086

[54] M. A. Tolstykh and V. V. Shashkin, *Vorticity-divergence mass-conserving semi-Lagrangian shallow-water model using the reduced grid on the sphere*, J. Comput. Phys. **231** (2012), no. 11, 4205–4233. MR 2911791

[55] P. A. Ullrich, *Understanding the treatment of waves in atmospheric models, I: The shortest resolved waves of the 1D linearized shallow-water equations*, Q. J. Roy. Meteor. Soc. **140** (2014), no. 682, 1426–1440.

[56] P. A. Ullrich and C. Jablonowski, *MCore: a non-hydrostatic atmospheric dynamical core utilizing high-order finite-volume methods*, J. Comput. Phys. **231** (2012), no. 15, 5078–5108. MR 2929934 Zbl 1247.86007

[57] P. A. Ullrich, C. Jablonowski, and B. van Leer, *High-order finite-volume methods for the shallow-water equations on the sphere*, J. Comput. Phys. **229** (2010), no. 17, 6104–6134. MR 2011d:76069

[58] US CLIVAR Scientific Steering Committee, *US climate variability & predictability program science plan*, Tech. Report 2013-7, US CLIVAR Project Office, 2013.

[59] R. L. Walko and R. Avissar, *The Ocean-Land-Atmosphere Model (OLAM), II: Formulation and tests of the nonhydrostatic dynamic core*, Mon. Weather Rev. **136** (2008), no. 11, 4045–4062.

[60] H. Weller, *Controlling the computational modes of the arbitrarily structured C grid*, Mon. Weather Rev. **140** (2012), no. 10, 3220–3234.

[61] D. L. Williamson, J. B. Drake, J. J. Hack, R. Jakob, and P. N. Swarztrauber, *A standard test set for numerical approximations to the shallow water equations in spherical geometry*, J. Comput. Phys. **102** (1992), no. 1, 211–224. MR 93d:86006 Zbl 0756.76060

[62] N. Wood, A. Staniforth, A. White, T. Allen, M. Diamantakis, M. Gross, T. Melvin, C. Smith, S. Vosper, M. Zerroukat, and J. Thuburn, *An inherently mass-conserving semi-implicit semi-Lagrangian discretization of the deep-atmosphere global non-hydrostatic equations*, Q. J. Roy. Meteor. Soc. **140** (2014), no. 682, 1505–1520.

[63] M. Zerroukat, N. Wood, A. Staniforth, A. A. White, and J. Thuburn, *An inherently mass-conserving semi-implicit semi-Lagrangian discretisation of the shallow-water equations on the sphere*, Q. J. Roy. Meteor. Soc. **135** (2009), no. 642, 1104–1116.

Received June 24, 2014. Revised May 26, 2015.

PETER MCCORQUODALE: pwmccorquodale@lbl.gov
Computational Research Division, Lawrence Berkeley National Laboratory, 1 Cyclotron Road, MS 50A1148, Berkeley, CA 94720, United States

PAUL A. ULLRICH: paullrich@ucdavis.edu
Department of Land, Air and Water Resources, University of California, Davis, 1 Shields Avenue, Davis, CA 95616, United States

HANS JOHANSEN: hjohansen@lbl.gov
Computational Research Division, Lawrence Berkeley National Laboratory, 1 Cyclotron Road, MS 50A1148, Berkeley, CA 94720, United States

PHILLIP COLELLA: pcolella@lbl.gov
Computational Research Division, Lawrence Berkeley National Laboratory, 1 Cyclotron Road, MS 50A1148, Berkeley, CA 94720, United States

Communications in Applied Mathematics and Computational Science

msp.org/camcos

See inside back cover or msp.org/camcos for submission instructions.

The subscription price for 2015 is US $85/year for the electronic version, and $120/year (+$15, if shipping outside the US) for print and electronic. Subscriptions, requests for back issues from the last three years and changes of subscribers address should be sent to MSP.

Communications in Applied Mathematics and Computational Science (ISSN 2157-5452 electronic, 1559-3940 printed) at Mathematical Sciences Publishers, 798 Evans Hall #3840, c/o University of California, Berkeley, CA 94720-3840, is published continuously online. Periodical rate postage paid at Berkeley, CA 94704, and additional mailing offices.

CAMCoS peer review and production are managed by EditFLOW® from MSP.

PUBLISHED BY

mathematical sciences publishers

nonprofit scientific publishing

http://msp.org/

Communications in Applied Mathematics and Computational Science

vol. 10 no. 2 2015